Published in final edited form as:

Cell Rep. 2021 September 28; 36(13): 109744. doi:10.1016/j.celrep.2021.109744.

Light-guided sectioning for precise *in situ* localization and tissue interface analysis for brain-implanted optical fibers and GRIN lenses

Anat Kahan[1,2], **Alon Greenbaum**[1,2,3], **Min J. Jang**[1], **J. Elliott Robinson**[1,4,5], **Jounhong Ryan Cho**[1], **Xinhong Chen**[1], **Pegah Kassraian**[1], **Daniel A. Wagenaar**[1], **Viviana Gradinaru**[1,6,*]

[1]Division of Biology and Biological Engineering, California Institute of Technology, Pasadena, CA 91125, USA

[2]These authors contributed equally

[3]Present address: Joint Department of Biomedical Engineering, North Carolina State University and University of North Carolina at Chapel Hill, Raleigh, NC 27695, USA

[4]Present address: Division of Experimental Hematology and Cancer Biology, Cincinnati Children's Hospital Medical Center, Cincinnati, OH 45229-3026, USA

[5]Present address: Department of Pediatrics, University of Cincinnati College of Medicine, Cincinnati, OH 45267, USA

[6]Lead contact

SUMMARY

Optical implants to control and monitor neuronal activity *in vivo* have become foundational tools of neuroscience. Standard two-dimensional histology of the implant location, however, often suffers from distortion and loss during tissue processing. To address that, we developed a three-dimensional post hoc histology method called "light-guided sectioning" (LiGS), which preserves the tissue with its optical implant in place and allows staining and clearing of a volume up to 500 μm in depth. We demonstrate the use of LiGS to determine the precise location of an optical fiber relative to a deep brain target and to investigate the implant-tissue interface. We show accurate cell registration of *ex vivo* histology with single-cell, two-photon calcium imaging, obtained through gradient refractive index (GRIN) lenses, and identify subpopulations based on immunohistochemistry. LiGS provides spatial information in experimental paradigms that use

*Correspondence: viviana@caltech.edu.

AUTHOR CONTRIBUTIONS

Conceptualization, A.K., A.G., and V.G.; methodology, A.K. and A.G.; software, A.K., A.G., J.R.C., P.K., and D.A.W; investigation, A.K.; resources, A.K., A.G., M.J.J., J.E.R, J.R.C., X.C., D.A.W., and V.G.; writing – original draft, A.K., and A.G.; writing – review & editing, A.K., A.G., M.J.J., J.E.R, J.R.C., X.C., P.K., D.A.W, and V.G.; visualization, A.K. and A.G.; supervision, V.G.

SUPPLEMENTAL INFORMATION

Supplemental information can be found online at https://doi.org/10.1016/j.celrep.2021.109744.

DECLARATION OF INTERESTS

The authors declare no competing interests.

optical fibers and GRIN lenses and could help increase reproducibility through identification of fiber-to-target localization and molecular profiling.

Graphical abstract

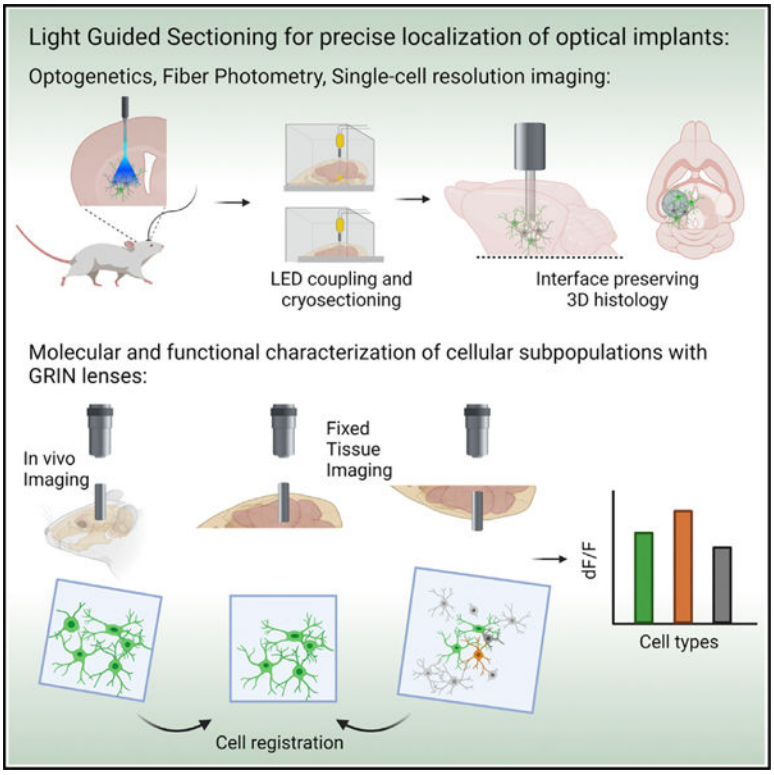

In brief

Kahan et al. describe a 3D histology method (LiGS) to investigate with high fidelity the vicinity of an intact optical implant (e.g., GRIN lenses and optical fibers). LiGS is compatible with immunohistochemistry and single-molecule imaging. With the use of two-photon microscopy, LiGS can also link the functional properties of cells to their molecular identity.

INTRODUCTION

Optical methods have become ubiquitous and indispensable in neuroscience research: they have considerably expanded the optical toolboxes available for controlling (optogenetics) (Fenno et al., 2011; Yizhar et al., 2011) and monitoring (Holtmaat et al., 2009; Goldey et al., 2014; Gunaydin et al., 2014; Jennings et al., 2019; Meng et al., 2019; Abdelfattah et al., 2019; Zou et al., 2014; Piatkevich et al., 2018) neuronal activity in awake animals. These methods use optical fibers to deliver and collect light from deep brain regions. Gradient refractive index (GRIN) lenses became popular for use in one- and two-photon, *in vivo*, single-cell calcium imaging because they provide optical access to deep brain regions (>1 mm). The common practice for histological detection following those experiments involves pulling out the optical implant (optical fiber or a GRIN lens) and sectioning the

tissue. Thus, the precise placement of the optical implant is lost despite its importance for the reliability and rigor of the placement. In addition, the removal of the implant disrupts the implant-tissue interface, leading to the loss of crucial experimental information. Furthermore, precise identification of the location of a GRIN lens can facilitate post hoc identification of individual regions-of-interest (ROIs) imaged at single-cell resolution and can open new opportunities for data collection and analysis, such as cell labeling and tracing.

To address that concern, we developed a histological method that preserves the implant-tissue interface, which enables three-dimensional (3D) investigation of the tissue below the implant with optional immunohistochemistry (IHC) labeling. The method (Figures 1A and 1B) keeps the optical implant firmly anchored to the skull so as not to perturb the interface. Then, we use cryosectioning to reach relevant layers of brain tissue under the implant. Cryosectioning (ventrally) allows the removal of soft and osseous tissue until the vicinity of the interface, within 300–500 μm, is reached. The end point of the sectioning is determined by coupling the implant to a light-emitting diode (LED) at its outer side. The light-distribution pattern through the soft tissue indicates the distance between the interface and the tissue surface during sectioning (Figure 1C). In this way, the coupled LED serves as a guide for sectioning, hence, our term “light-guided sectioning” (LiGS). After sectioning, the sample is processed, labeled, and optically cleared for a 3D investigation of the implant environment and placement. LiGS can also be used to quantify the distribution of recorded cells in two-photon imaging and to determine their molecular identity using supplementary IHC.

To demonstrate the versatility of LiGS, we applied the method to both optical fiber and GRIN-lens-implant experiments in mice. After monitoring genetically encoded calcium-indicator (GCaMP) activity *in vivo* via fiber photometry (FP), LiGS allowed us to correlate optical fiber positioning errors with calcium signal strength in the suprachiasmatic nucleus (SCN) and to visualize the glial scar formation from optical implantation via IHC showing increased expression of glial fibrillary acidic protein (GFAP). In GRIN-lens-implanted mice, we show how LiGS can add information to single-cell-resolution imaging. After two-photon GCaMP imaging, images acquired *in vivo* were registered to LiGS-processed tissue images in the striatum. Using IHC, we identified ARC- and c-Fos-expressing cells in the time-lapse GCaMP recording. We show that the subpopulations exhibited increased event rates after cocaine injection. Together, these data suggest that the LiGS method can help the neuroscience community improve experimental reproducibility, study the 3D implant-tissue environment, and gather valuable, complementary, postmortem data on individual cells imaged *in vivo* via optical implants.

RESULTS

Basic principles of LiGS

We introduce a methodology for accessing the tissue volume around and below an optical implant in a minimally invasive manner, allowing 3D histology of the implant-tissue interface in its original position. The primary pipeline includes four steps: (1) pre-treatment, (2) tissue slicing, (3) tissue clearing, and (4) imaging (Figure 1A). The first step, pre-

treatment, includes fixation in paraformaldehyde (PFA), followed by cryopreservation in 30% sucrose. The second step, tissue slicing, includes coupling an LED to the implant from the exposed, outer side and embedding it in a cryo-sectioning medium (Figure 1B). Cryo-sectioning is performed when the LED illuminates the tissue through the implant. Consequently, the LED is used as a light-guide to remove residual tissue (Figure 1A, ii). By observing the light pattern, the tissue thickness between the implant and the tissue surface can be estimated, which is needed to decide on the slicing endpoint (Figure 1C). The closer the tissue surface is to the implant, the narrower the light profile becomes, with a dramatic increase in peak intensity when the implant is ~300 μm from the surface. Light profiles using different optical-implant diameters–200- and 400-μm optical fibers and a 600-μm GRIN lens–are provided for reference (Figure 1D). Because the light profile changes during slicing and depends on the implant used, a Gaussian fitting to the light profile at different distances is presented, showing that the light profiles are relatively consistent between implants with the same diameter (Figure 1E, see also Figure S1 and method details). After sectioning, the sample retains the intact optical device; the distance between the implant and the tissue surface–up to 500 μm–is optimized to enable antibody (ab) penetration and clearing. During the third step, the sample is optically cleared with the fructose-based SeeDB method (Ke et al., 2013); we chose this method because it distorts the tissue volume minimally and maintains the fidelity of the implant-tissue interface, thus leaving the cellular morphology intact (Ueda et al., 2020). Lastly, the cleared sample is subsequently imaged from the exposed tissue side (i.e., upside-down). This position allows for 3D reconstruction of the optical implant interface, simultaneous determination of the optical implant placement, and investigation of the cellular marker expression in the surrounding area at a depth of up to 500 μm.

LiGS can identify GCaMP-expressing neurons recorded in FP with 3D IHC tissue staining

An additional improvement of this method is achieved by combining it with molecular cell identification using staining. For IHC ab staining, we used the 3D immunolabeling of large tissue samples protocol (iDISCO) (Renier et al., 2014) and skipped the pretreatment step to minimize tissue distortion (Figure 2A).

We first tested the benefit of using LiGS in FP experiments by correlating the precision of the fiber placement with signal strength. To focus exclusively on the effects of fiber placement on the FP signal, we used transgenic mice. We targeted a deep and small subpopulation of SCN neurons that express vasoactive intestinal peptide (VIP; SCN^{VIP}) by crossing VIP-cre mice to the Ai162 (GCaMP6s) mouse line. As the SCN^{VIP} population is highly responsive to light stimuli (Jones et al., 2018), we recorded *in vivo* FP signals from VIP × Ai162(GC6s) mice implanted with optical fibers during and after 15 s of exposure to ambient room light (Figure 2B). We performed classical slice histology. In most cases, the tissue was fragile and broke apart, and conclusions regarding the fiber location could not be achieved. Two slices (70 μm thick) allowed an estimation of the fiber location; however, the lack of the FP signal cannot be explained based on this two-dimensional (2D) histology (Figure 2C). Using the LiGS pipeline (Figure 2A), GFP-ab staining was used to amplify the GCaMP signal, and the cleared sample was subsequently imaged from the exposed tissue side. Based on the imaged 3D volume below the fiber location, we quantified the

cell population. The amplitude of fluorescence change (dF/F) from the SCN^{VIP} neurons ranged from 0% to 28% in response to light exposure (Figures 2D, 1, and 2E, 1). These responses corresponded with 270 and 30 stained cells, at average distances of 121 and 154 μm, respectively, based on the imaged volume (Figures 2D, 2, and 2E, 2; also Figure S2A). In addition to cell distribution under the implant, LiGS provided information in three dimensions, including the exact fiber orientation (dashed yellow line in Figures 2D, 2, and 2E, 2, middle). Digital sections in the XZ plane, simulating gold-standard histology, show only a few cells below the implant (Figures 2D, 2, and 2E, 2, right). LiGS, therefore, is superior precisely because it can identify how far the target is from the fiber edge and how it relates to the fiber's orientation.

Another benefit of precise implant localization is that it helps optimize the targeting coordinate in all three dimensions. Over multiple samples, we found a correlation between dF/F and the distance from the fiber edge to the center of the closest SCN (right or left), showing that greater fluorescence signals were correlated with more-precise fiber placements (Figure S2B; n = 12). Based on the existence of this correlation, we used the 3D information to optimize the targeting coordinates. This process increased the success rate of our SCN^{VIP} FP surgeries, quantified as the percentage of animals that yielded a detectable FP signal. By adjusting the coordinates over nine surgery sessions, the success rate increased from less than 50% to more than 75%, and the mistargeting distance dropped from 300 to 0 μm (Figure S2C).

LiGS and IHC labeling were used to map GCaMP expression after AAV injection. This application is shown with a Th-cre mouse, which was injected with AAV5.Syn.Flex.GCaMP6s in the ventral tegmental area (VTA). After performing the tissue-processing steps mentioned above, including the GFP-ab staining, the cleared sample was subsequently imaged from the exposed tissue side (Figure 2F). This positioning enabled simultaneous determination of optical implant placement and investigation of cellular-marker expression in the surrounding area at a depth of up to 500 μm (Figure 2G). Using IHC, we identified 220 cells, compared with only 34 cells in the GCaMP channel. A similar trend was demonstrated with dopamine transporter (DAT)-cre mice expressing GCaMP6f in the VTA. High-amplitude fiber photometry responses were correlated with a larger number of cells in the histology (Figures S2D–S2F). These examples demonstrate how combining LiGS with staining leads to a better understanding of fiber location, virus expression, and FP signal.

3D investigation of tissue-implant interactions using LiGS with IHC staining

LiGS offers a viable method for studying the damage inflicted by optical implants on the surrounding tissue. This subject is important because of the growing interest in glial cell function *in vivo* (Guo et al., 2017; Losi et al., 2017). Optical fibers implanted in the brain cause glial scar formation, which is also affected by experimental variables, such as surgical technique, animal health, stress, hormones, and other factors. Here, we investigated the expression of an astrocyte marker, GFAP, at the implant-tissue interface in the SCN. VIP-cre mice, crossed to Ai140 (GFP-tTA) or Ai162 (GCaMP6s) mice, were implanted with single or bilateral optical fibers. We used LiGS to image GFAP expression in the SCN

from both hemispheres (Figure 3A). We found an apparent increase in GFAP expression in the SCN at the location of the fiber edge (Figure 3B). Over five samples, the relative fluorescence (RF, ($RF = I_{implant} / [I_{implant} + I_{no\ implant}]$)) was calculated, where I is the intensity of the fluorescence in the SCN with and without the implant. We found that RF of the implanted side in GFAP was greater than that of GFP. The RF distribution of GFP was even (around 0.5; Figure 3C, yellow line), whereas the GFAP RF distribution was greater toward the implant side ($RF_{GFP} = 0.52 \pm 0.04$; $RF_{GFAP} = 0.67 \pm 0.03$ means ± SEM, $p = 0.036$, two-sample Kolmogorov-Smirnov test; Figure 3C). Inspired by previous studies that reported a decrease in astrocytic GFAP expression in the hippocampus of ovariectomized (OVX) female mice (Ma et al., 2016), we compared SCN GFAP expression from implant damage in intact versus OVX females. We found a significant decrease in GFAP expression in OVX females compared with intact females (Figures 3D and 3E), from 0.51 to 0.04 (a.u.) ($n_{intact} = 5$, $n_{OVX} = 6$). These differences in GFAP expression, visualized and quantified with LiGS, indicate that OVX diminishes post-implantation GFAP expression within the SCN. Other glial markers at the striatum implant site were tested for compatibility with the pipeline: Iba1 for microglial cells and additional astrocyte markers, such as s100β and estrogen-receptor type 1. If the ab does not provide sufficient penetration, LiGS can be combined with fluorescence *in situ* hybridization-hybridization chain reaction (FISH-HCR) staining up to 1 mm in tissue slices, followed by SeeDB clearing (Figure S3).

To conclude, these results show that LiGS is compatible with multiplexed IHC and FISH and demonstrate the benefits of using LiGS histology to investigate tissue-implant interactions.

Cell registration after single-cell-resolution imaging through GRIN lenses

After establishing the LiGS labeling protocol, either with multiplexed IHC or with FISH, we developed a protocol to match *in vivo* single-cell ROIs imaged with a two-photon microscope to post hoc LiGS histology. Four additional steps were added to the basic pipeline presented in Figure 1: *in vivo* volume imaging (z stack), post hoc staining, imaging through the GRIN lens, and cell registration (Figure 4A). After imaging fixed tissue from the exposed side, we identified two significant challenges during the cell-registration step: first, individual cell brightness differed between *in vivo* and fixed tissue, and second, the *in vivo* field of view (FOV) was smaller than that of the GRIN lens surface (~250 μm of the 600-μm diameter of the GRIN lens). Therefore, even if the tissue under the GRIN lens was exposed and imaged, it was not straightforward to locate the relevant cells or the sample working distance (WD), defined as the distance from the inner implant tip to the targeted cells inside the tissue (Figure 4B). To address that challenge, we imaged the fixed tissue through the GRIN lens in addition to imaging it from the exposed tissue side. This intermediate step narrows down the search space for cell registration because it images approximately the same volume as that of the *in vivo* imaging data. As a result, visually comparing the *in vivo* images with the intermediate z stack taken through the GRIN lens assisted in identifying landmarks for registration. In that case, the sample slicing steps require attention to the perpendicular orientation of the slicing relative to the GRIN lens and during imaging (Figures S4A–S4C; Method details). Note that because a specific volume

was imaged, some flexibility in the orientation is permitted without losing the ability to identify ROIs.

The cell-registration pipeline was developed using a dataset of six C57BL/6N mice expressing GCaMP in the striatum under a synapsin promoter. The pipeline included *in vivo* transient z stack imaging, followed by z stack imaging of the LiGS-processed tissue through the GRIN lens and the exposed tissue side. The averages of the transient imaging of the *in vivo* z stack optical sections and the z stack images from the tissue side were both registered to fit the fixed-tissue z stack images obtained through the GRIN lens, which thus served as anchors (Figures 4B and 4C). For registration, several neurons were identified and served as landmarks; three of these are indicated by yellow arrows (Figures 4C, S4D, and S4E; Method details). By registering individual sections along the z stack, a volume of 350 ×350 × 75 μm was matched (Figure 4D).

A few observations were considered in cell registration. First, the *in vivo* live imaging, which was performed for three minutes in each optical section, can be observed as either an averaged value (AVG) or a maximum intensity projection (MIP) (Figure 4E; mice 2 and 3). MIPs have greater contrast than the AVG images have, and processes can be visualized; however, registering cells using MIPs would lead to the loss of identification of modestly active cells. For example, neurons can be observed in the AVG *in vivo* image but are less visible using MIPs (Figure 4E, white arrows). Second, the averaged FOVs along the GRIN lens optical axis are usually ~70–75 μm from the GRIN lens surface (Figure 4E, right side), an obseravtion which assists in focusing the cell identification to specific sample WDs

Identifying the ROIs allowed us to quantify useful GRIN lens parameters, such as WDs and magnification. We found that the image WDs *in vivo* (distance from the outer GRIN lens surface during imaging *in vivo*; Figure 4B) were between 550 and 900 μm, similar to image WDs in fixed tissue (Figure 4F, 1). This suggested that tissue-processing steps had minor effects on the refractive index (~1.45–1.49). Image WDs *in vivo* correlated with sample WDs of 0–150 μm (Figure 4F, 2), defined as the distance from the inner GRIN lens tip to the targeted cells during post hoc imaging (Figure 4B). We also found that the GRIN lens magnification factor was between 2 and 1.4, with higher magnification values when the sample WD was small, i.e., very close to the inner GRIN lens surface (Figure 4F, 3). A scheme that summarizes these observations is shown in Figure 4F, 4.

Finally, we verified the registration of the cells, and for that purpose, we used an image similarity score (structural similarity index measure [SSIM], MATLAB [MathWorks]) to compare the *in vivo* GCaMP-expressing cells to the fixed-tissue images under the same conditions, i.e., imaged through the GRIN lens. We found that some bright *in vivo* cells could not be observed in fixed tissues (Figure 4G). Even with the loss of brightness, using the aforementioned registration process, an average of 87% ± 6% cells were identified over six samples. In each sample, 8–15 cells of 12–16 cells were identified in each optical section. With this high-performance cell-reconstruction ability, we aimed to correlate cell activity with cellular identity via LiGS histology.

Identification of molecular and functional cell-type after two-photon imaging and cell registration

Because LiGS is compatible with IHC, we aimed to expand its utility with single-cell registration of detected ROIs to reveal cellular identity. To do that, a post hoc IHC labeling stage was added to the previous pipeline (Figure 5A). We selected markers that have a broad expression in the striatum (Renier et al., 2014). Two C57BL/6N mice expressing GCaMP7b or GCaMP6s (under the synapsin promoter) were implanted with a GRIN lens (600 or 500 μm in diameter, respectively) in the striatum. These mice were imaged *in vivo* (z stack), followed by LiGS, iDISCO staining, clearing, and fixed-tissue z stack imaging through the GRIN lens and from the exposed tissue side. The first sample was labeled with the forkhead box protein P2 (FOXP2) ab. We acquired two channels for the fixed-tissue z stack imaging, one for GCaMP and another for FOXP2. Slight adjustments were needed to correct for chromatic aberrations in the two-photon setup, which was done based on autofluorescence marks (Figure 5B, asterisk, left). The correction success was tested on the rest of the z stack (Figure 5B, right; Video S1). Next, the cell registration pipeline (as presented in Figure 4) was applied. This step allowed us to compare the GCaMP-active cells ($GCaMP^+$) recorded *in vivo* with the stained population and, hence, to identify co-labeled cells. Here, we present examples from two samples, showing two representative optical sections along the z stack for each sample (Figure 5C). In the aforementioned sample labeled with FOXP2, we identified three $GCaMP^+/FOXP2^+$ cells of 22 $GCaMP^+$ cells (image WD = 485 μm). In the other optical section (image WD = 755 μm), none of the $GCaMP^+$ neurons were also $FOXP2^+$. The few identified $GCaMP^+/FOXP2^+$ cells can be explained by the fact that FOXP2 is mainly a developmental-related marker linked to vocalization, neither of which would be expected to be highly correlated with striatal activity in head-fixed adults. The second sample was labeled with an ARC ab, an immediate early gene (IEG). This sample was used to test for the ARC labeling technique, and no correlation between *in vivo* activity and ARC staining was expected. This labeling yielded two and four co-labeled cells of 28 and 26 $GCaMP^+$ neurons in each optical section, respectively (Figure 5D). We demonstrated the pipeline with IHC labeling using non-transgenic mice, to emphasize the flexibility if other animal models are in use. In addition, neuronal subpopulations can also be identified using cre lines. Figure S5 shows pan-neuronal GCaMP expression combined with cre-dependent tdTomato using Drd1-cre and Drd2-cre mice. Whether IHC or cre-dependent labeling is used, the ability to co-label active neurons post hoc is a desirable feature.

Combining GCaMP single-cell resolution responses to drug stimuli *in vivo* with post hoc labeling

Next, we compared the activity patterns of GCaMP-active population with a subset of $ARC^+/c\text{-}Fos^+$ neurons. To induce activity, we used cocaine stimulation, which increases ARC expression in the striatum (Tan et al., 2000; Li et al., 2018). The compatibilities of the ARC and c-Fos abs were tested on a 500-μm brain slice that included the striatum (Figure S6). A C57BL/6N mouse was injected with AAV9.hSyn.GCaMP6 and implanted with a GRIN lens (500 μm diameter) in the striatum. The behavioral scheme was as follows: after habituation to head fixation, a full z stack was imaged using a two-photon microscope. The following day (day 1), the mouse was injected with saline and, on day 2, with cocaine. The calcium signal was recorded for 10 min, beginning 10 min after injection,

assuming that changes in GCaMP activity would correlate with the quick rise of ARC mRNA expression (Vassilev et al., 2020; Guzowski et al., 2005). After imaging, the mouse was perfused to preserve ARC expression related to the neural activity (25–30 min after cocaine injection; Figure 6A). *In vivo* imaging was performed at an image WD of 870 μm, corresponding to a sample WD of 84 μm (Figure 6B). Cell registration of the GCaMP signal was performed. The transformation was applied to the ARC-labeled and c-Fos-labeled images. Of 43 $GCaMP^+$ neurons, seven neurons were identified as $GCaMP^+/ARC^+$ (bright white masks in the ARC channel). Two of those neurons were also found to be $c\text{-}Fos^+$ ($GCaMP^+/ARC^+/c\text{-}Fos^+$, bright white masks in the c-Fos channel). Details regarding the identification process can be found in the Method details section and in Figure S6. A map of the calcium-dependent traces after the saline and cocaine injections is presented in Figure 6C, showing a general increase in the event rates. Comparing the event rates of the entire cell population from the saline versus the cocaine injection reveals an increase from 1.39 ± 0.12 to 1.96 ± 0.14 events/min ($p = 0.0001$, Kruskal-Wallis test, see also Video S2). $GCaMP^+/ARC^+$ neurons show an increase from 1.50 ± 0.31 to 2.07 ± 0.30 events/min, and the two $GCaMP^+/ARC^+/c\text{-}Fos^+$ neurons had increased event rates on average from 1.004 ± 0.001 to 2.21 ± 0.70 events/min (Figures 6D and 6E). Three representative cells from each group highlight the increased event rates from the cocaine (Figure 6F). The two subpopulations show a loss of statistical significance compared with the prior analysis for the entire population. To understand whether this was due to a reduced number of cells or to a specific characteristic, we calculated the event rate in a small group of neurons ($n = 7$), $GCaMP^+/ARC^-$, arbitrarily chosen, and found a similar increase in the event rate as a result of the cocaine injection but also a loss of significance (1.19 ± 0.23 to 1.94 ± 0.24 events/min; Figure S6). It is possible that other IEGs take part in the increased activity or that a longer waiting time is required for broader protein expression. This example demonstrates the potential of our method for isolating and comparing the activity patterns of specific cellular populations. This feature can be used to reveal the cellular identity of cells participating in a complex activity without the need for transgenic mice.

DISCUSSION

LiGS is a 3D histology method that aims to localize implanted optical devices with cellular resolution. Here, we introduced the method and demonstrated its applicability and advantages: accurate and precise 3D fiber placement, IHC for 3D GCaMP observation and tissue-implant interface investigation, and registration of single cells recorded during *in vivo* two-photon imaging to 3D histological analysis.

In vivo studies that involve light delivery and collection for deep, small, or fragile brain structures require high precision placement of optical elements and the ability to profile the tissue post-mortem molecularly. For example, fiber photometry investigation of the small (~400 μm diameter, ~700 μm long) and deep (−5.5 dorsal-ventral [DV]) SCN (Figure 2) requires the implantation of long optical fibers that cut across a significant brain volume (Mazuski et al., 2018; Fernandez et al., 2020; Jones et al., 2015; Mei et al., 2018). In our experience, regular histology in the SCN was challenging because of tissue disintegration that led to a <50% success rate in identifying the implant location when performing classical histology. Even in that successful fraction, regular histology can be inaccurate because the

fiber placement is estimated based on its track. Precise placement is critical in experiments in which two adjacent brain areas share the same cellular population, and the recorded signal might originate from a brain region other than the one being targeted. With LiGS, we achieved successful histological analysis in >85% of the 31 total samples, with precise fiber placement assured by its retention in the tissue. In the 15% of samples that failed, the SCN was not found, probably because of excessive slicing or its detachment from the hypothalamus during dissection when the optic nerve pulls on the ventral hypothalamus. Therefore, LiGS 3D localization facilitates the accurate investigation of deep and small brain regions.

LiGS relies on the fact that the SeeDB clearing and the methanol-free iDISCO staining protocol preserve the sample size; therefore, the interface between the implant and the tissue is preserved. GFAP expression at the implant site was previously presented, showing increased GFAP expression in astrocytes after injury (Sofroniew and Vinters, 2010; Pflüger et al., 2020; Xie et al., 2014; Campbell and Wu, 2018; Sych et al., 2019; Park et al., 2017). The fact that samples from OVX females showed a significant reduction in GFAP expression in the SCN, when compared with intact females, is probably related to the neuroprotective role of estrogen in GFAP-expressing astrocytes (Ma et al., 2016) (see also Figure S3 for estrogen receptor 1 and GFAP colocalization). Because LiGS is compatible with additional markers related to glial scar formation, further investigation can be done to understand scar formation and brain injury with LiGS. We hope that LiGS and its future modifications will open avenues to study and evaluate approaches to integrate implants into other tissues in a better way.

The greatest advantage of LiGS is the ability to match ROIs that were captured *in vivo* via two photons to fixed-tissue 3D histology images. This gave rise to an important technical observation: we identified that, when using a GRIN lens, the sample WDs are in the range of 0 to 150 μm (see Figure 4F). That fact should be considered when injecting viruses and placing the GRIN lens at its target location. In addition, LiGS can be compatible with fast techniques for volume imaging, such as a Bessel beam (Lu et al., 2017), which, by definition, would benefit from 3D histology.

We used three antibodies to demonstrate how LiGS can identify subpopulations of neurons. However, in some situations, deep ab labeling is not feasible because of limited penetration. To address that issue, one can combine cre-dependent mice with cre- and non-cre viruses (Figure S5; see also Luo et al., [2011]). This approach may be beneficial, although the availability of transgenic animals or transgene delivery cargos depends on the target and species.

Combining histology with functional *in vivo* imaging data links molecularly defined cell types with functional aspects of the neuronal response. Few papers have demonstrated that ability (Khan et al., 2018; Wilson et al., 2017; Langer and Helmchen, 2012; Keller and Martin, 2015; Lovett-Barron et al., 2020; von Buchholtz et al., 2021); recently, however, Xu et al. (2020) demonstrated registration between two-photon imaging and post hoc FISH labeling using a GRIN lens, which adds an optical aberration and, therefore, complexity in cell registration. Interestingly, LiGS and the method demonstrated by Xu et al. (2020)

perform similarly, by identifying a similar percentage of fluorescent cells (89% in Xu et al. [2020] and 87% here). Xu et al. (2020) used a similar methodology to match cells *in vivo* and in the fixed tissue by imaging the volume before and after perfusion. That approach was performed in non-cleared tissue before removing the GRIN lens for thin slicing and FISH labeling. In contrast, LiGS relies on identifying the implant location by interrogating the entire volume below the implanted optical device using tissue clearing. This fact makes the cell registration process easy and flexible, without the need for *a priori* calibration steps (as used in Xu et al. [2020]), and the user can digitally change the orientation of the optical implant to any angle. On the other hand, with the current IHC technique used in LiGS, the number of molecular identifying markers is limited. Although LiGS was developed for 3D histology, LiGS is also compatible with thin slices for multiplexed FISH labeling. LiGS slicing and imaging approaches can also improve the methodology presented by Anner et al. (2020) for one-photon GRIN lens calcium imaging and cell reconstruction.

In the future, LiGS can be used in experiments that combine optical fibers with electrophysiological probes, such as FP in conjunction with local field potential recordings (Patel et al., 2020) or optogenetics in conjunction with extracellular recordings (optrodes) (Biran et al., 2008). Lately, slice-recorded electrophysiology data have been combined with information on cell morphology by injecting biocytin and then conducting high-resolution fixed-tissue imaging (Gouwens et al., 2019). Correlating cell morphology with activity can be addressed through LiGS by recording GCaMP activity through a GRIN lens and using additional viruses to track cell morphology (Lin et al., 2018) for post hoc identification. In light of our findings regarding ARC- and c-Fos-labeled neurons, it will be interesting to examine other IEGs and assess any correlations between labeled cells and GCaMP activity.

LiGS could greatly benefit from two technological advancements. First, an improved clearing and labeling method that does not change the physical volume of the tissue during processing and also provides ab depth penetration at the millimeter scale. These techniques would facilitate LiGS usage with applications that require preserving larger volumes of tissue under the fiber, such as retrograde labeling. Second, an automatic method of providing the LiGS user with feedback on how far the current section is from the fiber tip during sectioning would speed up the acquisition of the technique. Finding the right end point when sectioning might be the most challenging aspect when training new users on LiGS.

LiGS can be easily adopted by any standard-equipped neuro-biological laboratory and used in various animal models; thus, we anticipate that there will be broad benefits to the neuroscience community from the increased precision and additional layers of information that LiGS provides.

STAR★METHODS

RESOURCE AVAILABILITY

Lead contact—Further information and requests for resources and reagents should be directed to and will be fulfilled by the lead contact, Viviana Gradinaru (viviana@caltech.edu).

Materials availability—This study did not generate new unique reagents

Data and code availability—The datasets supporting the current study have not been deposited in a public repository but are available from the corresponding author upon reasonable request.

All original code has been deposited at github.com and is publicly available as of the date of publication. DOIs are listed in the key resources table

Any additional information required to reanalyze the data reported in this paper is available from the lead contact upon request.

EXPERIMENTAL MODEL AND SUBJECT DETAILS

Animal husbandry and experimental procedures involving animal subjects were conducted in compliance with the Guide for the Care and Use of Laboratory Animals of the National Institutes of Health and approved by the Institutional Animal Care and Use Committee (IACUC) and by the Office of Laboratory Animal Resources at California Institute of Technology under IACUC protocols 1730 and 1739.

Mice—Mice used in this work include VIP-IRES-cre (Jackson Laboratory Stock, JAX, 010908), crossed to Ai162 (GCaMP6s reporter line, JAX, 031562), or Ai140 (GFP reporter line, JAX, 30220). A doxycycline diet was used to suppress expression until 2–4 weeks before surgery. VIP x Ai140 or VIP x Ai162 mice were used for histology (2 males and 11 females, 9–10-month-old). We also used: TH-cre (EMMA, Ted Ebendal, 254, one male, 8-month-old), DAT-cre (JAX, 6660, Two males, 6–8 month-old), C57BL/6N (Charles River, C57BL/6NCrl, 22 males, 6 – 10-month-old), Thy1-YFP (JAX, 3782, one male, 5 month-old), Drd1-cre (JAX, 030989-UCD, one male, 9 month-old), and Drd2-cre (JAX, 032108-UCD, one male, 5 month-old). Animals were group-housed (two to four per group) for SCN^{VIP} FP experiments or singly housed for two-photon experiments and DAT-cre reward experiments, in a vivarium, on a 12-hour light/dark cycle with *ad libitum* access to food and water. Fluid-restricted animals for two-photon habituation or reward experiments were singly housed, and their water access was limited to 1.5 ml/day. These mice were weighed daily and were returned to *ad libitum* water access if their weight decline was > 10% of their pre-restriction weight. Mice were excluded from the entire experiment if there was no dynamic photometry signal or no two-photon signal three or six weeks after surgery, respectively.

METHOD DETAILS

Surgery—*Stereotaxic viral vector injections* were made in mice anesthetized with isoflurane (5% induction, 1%–1.5% maintenance) and placed on a stereotaxic frame (942, David Kopf Instruments, CA, USA). An incision was made to expose the skull, including bregma, lambda, and the target sites. Stereotaxic coordinates were measured from bregma and were based on The Mouse Brain Atlas (Cetin et al., 2006; Franklin and Paxinos, 2004). A craniotomy hole was drilled above the target and injected with a virus (if applicable), as detailed in Table S1. The virus was injected at a rate of ~80 nl/min using a blunt 33-gauge

microinjection needle within a 10 mL microsyringe (NanoFil, World Precision Instruments, WPI) by an UltraMicroPump (UMP3–4, WPI), controlled by a pump controller (Micro4, WPI).

Fiber photometry (FP)—Following virus injection (if applicable), an optical fiber with a cut length of 3, 4, or 7 mm and diameter of 400 μm (MFC_400/430–0.48_3/4/7mm_ZF1.25_FLT, NA = 0.48, Doric lenses, Quebec, QC, Canada) was firmly mounted to a stereotaxic holder. The optical fiber was inserted into the striatum at a 0° angle, into the VTA at a 20° angle, or above the SCN from both the left and right hemispheres, at a 13° angle. For the SCN, two 7 mm fibers were implanted to improve the probability of successfully targeting this structure. A thin layer of metabond (Parkel) was applied to the skull surface to secure the fiber. In addition, a thick layer of black dental cement (JET denture repair powder and liquid) was applied to secure the fiber implant for FP recording. We iterated the FP coordinates for the SCN based on the LiGS histology results.

Two-photon—Following virus injection, a 500 μm or 600 μm diameter GRIN lens (GLP-0584, GLP-0673, Inscopix, Palo Alto, CA; Drd-cre; Figure S5; 500 μm diameter GRIN lens, NEM-050–30-10–920-S-2.0p, GRIN Tech) was firmly mounted to a stereotaxic holder. The GRIN lens was then inserted into the striatum (two sets of coordinates used: AP +1.0 mm, ML ± 1.3 mm, DV −3.5 mm, or AP: −0.1, ML: −1.5 DV: −2.7, from either the left or the right side) and positioned at the same height as the highest viral injection site or 0.15 mm above. Next, a thin layer of metabond (Parkel Inc) was applied to the skull surface to secure the GRIN lens. In addition, a thick layer of black dental cement (JET denture repair powder and liquid) was applied to secure the GRIN lens and to attach a customized head-fixing ring (stainless steel, 5-mm inner diameter, 11-mm outer diameter) around the GRIN lens to allow positioning and restraint of the animal during two-photon illumination. A thin layer of superglue was also used on the lower surface of the ring. After dental cement placing and curing inside the ring, the area above the GRIN lens was protected using a small piece of parafilm, covered with a layer of Kwik-Sil (WPI).

Table S1 summarizes all the different brain surgeries that took place in this work.

OVX—Each mouse was given a single dose of ketoprofen 5 mg/kg s.c. and sustained-release buprenorphine at 1 mg/kg s.c. The mouse was then anesthetized with 1%–5% isoflurane in an induction box followed by maintenance on a nose cone and remained on a heating pad throughout the surgery. A small dorsal midline incision was made over the abdomen. The abdominal cavity was entered via a blunt puncture through the abdominal wall. The ovary was dissected. The fat pad and tissue were returned to the abdominal cavity, and the abdominal wall was closed with 4–0 absorbable multifilament sutures in an interrupted pattern. The process was repeated on the opposite side through the single incision. The skin incision was closed with surgical wound clips or sutured with a monofilament 4–0 suture in an interrupted pattern. Bupivacaine (1 mg/kg of 0.25% solution) was applied subcutaneously to the wound margins before closure. Mice received 30 mg/kg ibuprofen *ad lib* (20 mg per 100 mL water) for at least five days. For all OVX females, surgery success was verified by collecting vaginal smears for at least ten days, showing either diestrus or metestrus states. OVX females (n = 6) were perfused 3–3.5 months after surgery.

All mice were given 1 mg/kg sustained-release buprenorphine and 5 mg/kg ketoprofen s.c. Intraoperatively and received 30 mg/kg ibuprofen p.o. in their home cage water for at least five days postoperatively for pain. Mice were allowed a minimum of 14 days for surgical recovery before participation in behavioral studies.

Fiber photometry recording—FP is a method for measuring population calcium-dependent fluorescence from genetically defined cell types in deep brain structures using a single optical fiber for both excitation and emission in freely moving mice. A detailed description of the system can be found elsewhere (Cho et al., 2017). Briefly, our system employed a 490 nm LED for fluorophore excitation (M490F1, Thorlabs; filtered with FF02–472/30–25, Semrock) and a 405 nm LED for isosbestic excitation (M405F1, Thorlabs; filtered with FF01–400/40–25, Semrock), which were modulated at 211 Hz and 531 Hz, respectively. Two systems were used for recording, both controlled by a real-time processor (System 1: RX8–2; System 2: RZ5P, Tucker-Davis Technologies), and delivered to the implanted optical fiber via a 0.48 NA, 400 μm diameter mono-fiber optic patch cable (MFP_400/430/LWMJ-0.48_2 m_FC-ZF1.25, Doric Lenses). The emission signal from isosbestic excitation, which has previously been shown to be calcium-independent for GCaMP sensors (Lerner et al., 2015; Kim et al., 2016), was used as a reference signal to account for motion artifacts and photo-bleaching. Emitted light was collected via the patch cable, collimated, filtered after passing through a focusing lens (System 1: MF525–39 filter, Thorlabs, 62–561 focusing lens, Edmunds Optics; System 2: Mini Cube FMC6, Doric Lenses), and detected by a femtowatt photoreceiver (Model 2151, Newport). Photoreceiver signals were demodulated into GCaMP and control (isosbestic) signals, digitized (sampling rates: System 1: 382 Hz; System 2: 6 Hz), and low-pass filtered at 25 Hz using a second-order Butterworth filter with zero phase distortion. A least-squares linear fit was applied to align the 405 nm signal with the 490 nm signal. Next, the fitted 405 nm signal was subtracted from the 490 nm channel and then divided by the fitted 405 nm signal to calculate dF/F values.

***In vivo* two-photon imaging—**All *in vivo* two-photon imaging sessions were conducted with a custom-built microscope, designed with the support of the Caltech Neurotechnology Laboratory. Briefly, a pulsed femtosecond laser beam at 940 nm, coming from a Ti:Sapphire laser system coupled with OPA (Insight DS+, Spectra-Physics, CA), passed through a beam expander (75:50) and an iris (SM1D12C, Thorlabs) set to 3 mm. An XY galvanometer (Cambridge Technology) was placed before a scan lens (LSM54–1050, Thorlabs) and a tube lens (AC508–200-B-ML, Thorlabs). An 805 nm shortpass dichroic (DMSP805SP, Thorlabs) was used to allow simultaneous near-IR visualization along with two-photon excitation. A 75-mm tube lens achieved Near-IR visualization for sample placement (AC508–075, Thorlabs) directed to an HDMI-output camera (HD205-WU, Amscope, IMX178, Sony). A 500–700 nm reflecting dichroic (T600/200dcrb, Chroma) was used to split two-photon excitation and emission paths. Power was measured after a 20X/0.5 NA objective (Olympus, UPLFLN20XP) and set to be 40–140 mW, based on the imaging quality. Photons were collected using collective optics (AC508–100-A, f = 100mm, at z = 100 mm from BA, most convex side facing sample and a pair of LA 1131, f = 50mm at z = 150 mm and z = 156 mm from the back BA, convex sides facing each other) and a 680 nm short-

pass filter (et680sp-2p8, Chroma) into a photomultiplier (Hamamatsu H10770PA-40). The stage XY adjustment and microscope focus were controlled by motorized linear actuators (Z825B, Thorlabs). The laser intensity was controlled by the rotation of a half-lambda waveplate (Thorlabs AHWP05M-980) relative to a Glan polarizer (Thorlabs GL10-B), using a motorized rotation stage (Thorlabs PRM1/Z8). Imaging data collection was controlled by an FPGA DAQ board (National Instruments 7855R) and a custom-written Labview interface. Laser safety during imaging was controlled by an electromechanical shutter (Uniblitz VS25, Vincent Associates). Image frame size varies with the GRIN lens properties and the field of view. Images were taken at 256 lines/frame at 13 μs dwell time, producing a frame rate of 1 Hz for *in vivo* z stack or 4 Hz for experiments involving saline or cocaine administration, where a higher temporal resolution was needed.

Behavioral assays

Light-exposure experiments: Mice were placed in their home cage and, during the dark phase, were exposed to 15 s of ambient room light six times, with 30 s of dark separating each exposure. A light sensor based on a GL5528 photoresistor was built with an Arduino UNO (Young, 2018). TTL pulses were sent to a TDT processor when resistance was low, indicating dark (the exact value was defined by the light conditions in the specific behavioral room and the sensor). From the TTL input, the exact timings of the light stimuli were extracted and averaged.

Reward consumption: During the sucrose consumption assay, mice were given free access to 50 mL sucrose (5% w/v) rewards delivered via a lick port in a mouse modular test chamber (Model 80015NS, Lafayette Instrument Company) placed within a light-attenuating box and controlled by ABET II software (Lafayette Instrument Company). The number of licks at the lick spout was measured with an optical lickometer in the lick port. After three days of habituation, mice were placed in the test chamber for 15 minutes while the FP signal was recorded. Sucrose consumption was quantified by measuring the timing and number of licks.

Two-photon behavioral assay: Training started at least two months after the surgery to ensure full recovery and bright imaging. Before imaging, water-restricted mice were habituated to the head-fixed position for at least five days in a custom-built transparent plastic tube (4.5 cm diameter). For each animal, a transient z stack was imaged while the animal was head-fixed and receiving water reward. No specific increase in signal was correlated to water consumption. The z stack imaging, three minutes in each optical section, was taken at steps of 15 or 5 μm for Inscopix GRIN lenses (500 or 600 μm diameter) or GRIN tech lenses (500 μm diameter), respectively, based on their optical properties under the two-photon microscope. When the volume imaged required a session longer than an hour, the imaging was split over several days, as needed. We ensured that the GRIN lens was perpendicular to the imaging plane by looking at the GRIN lens surface with a bright field. Adjustments were made by tilting the microscope head in one dimension (X, as allowed by our microscope set-up) or by tilting the mouse holder in the other dimension (Y). The GRIN lens was considered perpendicular when all edges of the GRIN lens were in focus. Thus, the

orientation of the head should be consistent throughout all imaging sessions. The orientation steps are necessary for the cell registration steps.

Two-photon imaging after saline or cocaine administration: We selected one optical section that was both relatively highly active and not too close to the GRIN lens surface to allow better staining penetration in the fixed brain. Ten minutes after i.p. injection of saline or cocaine (8 mg/Kg), the chosen optical section was imaged for 10 minutes, for two consecutive days. At the end of the cocaine imaging session, the mouse was perfused 25–30 minutes after the injection.

Tissue preparation—After perfusion (20 mL 1 × PBS followed by 20 mL 4% PFA), the implant was kept intact; the skin was gently removed without holding the implant, and the lower jaw was cut off. The remaining skull, including both brain and implant, was placed in 4% PFA for two days and washed in PBS. For cryo-protection, samples were then placed in 15% and 30% sucrose solutions for one day. For coupling, samples were placed in disposable embedding molds (22 × 22 mm, 70182, EMS) with OCT (Tissue-Tek Compound, Sakura Finetek) and were frozen with ethanol/dry-ice bath (−78°C). Brains were maintained in an upright orientation so that the outer surface of the optical device faced upward unless the implant was angled. In those cases, the brain was positioned such that the optical implant was perpendicular to the cube during freezing. It is important to ensure that OCT does not cover the outer side of the optical fiber. If it does, the OCT can be removed gently with a razor. However, extra care should be taken with GRIN lenses because any damage to the lens will prevent imaging through it. After the intact brain was embedded in OCT, a 5 mm LED (Chanzon, yellow) was placed directly above the optical device and secured with additional OCT. Direct contact between the LED and the optical device tip should be kept to allow reproducibility. To give the brain–OCT cube a flat surface, a larger embedding mold (22 × 40 mm, 70184, EMS) was filled with OCT while the brain (with the coupled LED) was placed upside down in it. This created a large, stable OCT cube that included the sample and the coupled LED. At the last step, the sample was cut on one side to expose the LED wires and stored at −80°C until used (see Method videos S1, S2, S3, S4, S5, and S6).

Light-guided cryo-sectioning—Brains in OCT were sliced in a cryostat from the bottom in 20–100 μm steps. The LED was turned on when needed. To ensure a repeatable light intensity, we used a power supply (DG1022, RIGOL) set to 2.1 V. We used the profile of the light spread to define the sectioning endpoint (see main text). Determining the correct endpoint required some iterations. Overall, one should practice sectioning in a way that will allow the relevant tissue to be preserved. We tested several methods for this: First, we coupled the optical device to short “legs” (piano wires, Precision Fiber Products, Inc., SMWL-004–01) positioned at a known distance from the surface of the optical device; sectioning was stopped when the wire became visible. However, the wires can cause tissue damage. Second, we attempted to develop an algorithm based on analyzing the images taken during sectioning. For each sample, photographs of the cryosectioning were taken every 50 μm with a cell-phone camera (Camera +2, iso 32, exposure 1/20 and 1/200) and registered to each other (MATLAB, using SIFT package). Finally, we used manual observation of the tissue: after the scattered light becomes sharp, sectioning continues in small steps (20–50

μm) until a sharper light profile is found or a shaded area is seen in the fiber location when the LED is turned off (Figure S1). In order to identify the distance of each photograph, the sample was cleared, and the distance between the fiber tip and the tissue surface was measured and was retroactively used to couple an image with a distance (Figure 1E). The process was repeated for all samples. A two-dimension Gaussian fit was applied to the light distribution. Amplitude and the mean Sigma were plotted against the distance from the implant for each implant. We found the last method to be the most efficient for 500 to 600 μm implants. For smaller diameters, using this approach ended up with a thinner layer of tissue below the implant, which in some cases was not sufficient. When required, sections close to the endpoint were kept for imaging but were otherwise disposed of. After sectioning, samples were left at room temperature (RT), allowing the OCT to melt gradually. Samples were then gently placed in a tube and washed with 1 × PBS solution.

Staining and clearing

IHC: After sectioning, brains were put in 4% PFA (RT) for 1–3 hours for additional fixation and washed with 1X PBS afterward. The staining protocol was adapted from the iDISCO protocol, without the pretreatment step [20], as follows: The samples were incubated for two days at 37°C in Permeabilization solution (500mL: 400mL PTx.2, 11.5g of Glycine, 100mL of DMSO. 1L PTx2: 100mL PBS 10X, 2mL Triton X-100), followed by two days in Blocking solution (50mL: 42mL PTx.2, 3mL of Donkey Serum, 5mL of DMSO) at 37°C. Next, the sample was incubated with primary antibody at 1:200 or 1:400 concentrations for 5–7 days in PTwH/5%DMSO/3%donkey serum at 37°C (PTwH, 1L: 100mL PBS 10X, 2mL Tween-20, 1mL of 10mg/mL Heparin). After washing at room temperature (RT) until the next day, samples were incubated in secondary antibody in PTwH/3% donkey serum at 37°C for 5–7 days (1:200, GFAP-ch ab4674 1:400). Lastly, samples were washed with PTwH at RT until the next day. IHC staining with the modified iDISCO protocol is sufficient for depths up to ~700 μm. The iDISCO protocol contains a list of antibodies that penetrate well. Before staining the light-guided cryo-sectioned brain, we validated the staining method and antibodies (GFAP, Iba1, PR, Esr1, see List of Materials) in 300–500 μm sections and found an even distribution of labeling (see Figure S3). Any new antibody should be tested first in a thick section (300–500 μm) at the relevant brain region. The new antibodies should be checked on a LiGS sample (half brain with skull) as well. If the antibody does not provide sufficient penetration, LiGS is compatible with fluorescence *in situ* hybridization (FISH)-HCR staining up to 1 mm in tissue slices (Figure S3A).

FISH-HCR: RNA fluorescence *in situ* hybridization (FISH) was performed by adapting hybridization chain reaction (HCR) (Choi et al., 2014). The probes were designed using custom-made scripts (Patriarchi et al., 2018) and produced by IDT. Once the whole brain had been prepared via LiGS, the OCT block was thawed, and the tissue was washed 2–3 times with 1 × PBS at room temperature. Hybridization was performed in a hybridization mixture (2 × SSC, 10% formamide, 1% Tween-20, 20 mM ribonucleoside vanadyl complex, 0.1 mg/ml salmon sperm DNA, and 10 nM of probes) at 37°C for 1–2 days. Next, the tissue was washed out with a wash buffer (2 × SSC and 10% formamide) and subsequently with 2 × SSC twice for 20 min each at 37°C. Hybridization chain reaction for signal amplification was performed in amplification mixture (60 nM hairpins (Molecular Technologies) in 2 ×

SSC) overnight at room temperature. Using FISH-HCR we were able to stain up to ~250 μm in a full sample (brain with skull).

Clearing: After staining, samples were cleared using the SeeDB clearing method [18]:

SeeDB recipe: D(−)-fructose was completely dissolved in distilled water at 65°C in 50 mL conical centrifuge tubes. After cooling to 25°C, α-thioglycerol was added to give a final concentration of 0.5% to prevent Maillard reaction.

	Composition		
	Fructose	**Solvent**	**α-thioglycerol**
20% w/v	4 g	add distilled water to make	100 μl
40% w/v	8 g	a total volume of 20 ml	
60% w/v	12 g		
80% w/v	16 g		
100% w/v	20 g		
SeeDB	20.25 g	add 5 ml distilled water	

- 5 mL of distilled water were added before fructose to assist the dissolving process.
- SeeDB should be freshly prepared.
- SeeDB solutions should not be kept at 65°C too long (> 5 h) because fructose will gradually caramelize.

Clearing steps

- The sample was incubated in 15–20 mL of 20% (w/v) fructose solution in a 50 mL conical tube and placed on a shaker 4–8 h at 25C.
- The sample was incubated in 40% (w/v) fructose for 4–8 h as above.
- The sample was incubated in 60% (w/v) fructose for 4–8 h.
- The sample was incubated in 80% (w/v) fructose for 12 h.
- The sample was incubated in 100% (w/v) fructose for 12 h.
- The sample was incubated in ~20 mL SeeDB for 24–48 h.

Based on the volumetric imaging, we did not observe damage to the coating of the GRIN lens due to this processing.

Sample mounting—For an air objective lens imaging, we used iSpacer (0.5, 1.0, 3.0, 7.0 mm, IS011, IS013, IS014, SunJin lab, used as needed), and 22 × 30 glass microscope coverslips (16004–344, VWR) were placed on both sides. 1 mL pipette tips were cut to ~1 cm pieces and were used to stabilized the sample (Figure S4).

For an immersion objective lens imaging (used in Figures 6 and S6), we used a 5 cm diameter Petri dish and created a template for the head-fix ring using a new ring and applying Kwik-Sil (WPI) glue around it. The sample is mounted with the used and fixed ring placed in the template for stability (Figure S4). Here greater care should be taken for keeping the sample parallel. Taking a large Z stack can help to adjust the angle later in the analysis using 3D software, as Imaris.

Histological imaging—Histological images were obtained with a Keyence BZ-X fluorescence microscope (for regular 2D histology), a Zeiss LSM 880 confocal microscope (with Airyscan, when applied), or a custom-built two-photon microscope. The Zeiss 880 confocal microscope was used for all optical-fiber Z stack/volume imaging with a 10X air objective (Plan-Apochromat 10X/0.45). Zoom was adjusted up to 2 and images were taken at 5 or 10 μm steps. For Figure 6A; 25X immersion lens was used (Plan-Apochromat 25X/0.5 Imm Korr DIC). Whenever comparative quantification was used, laser intensities and filters were matched. Two-photon Z stack images were taken at 512 lines/frame, 125 μs dwell time, with laser wavelengths of 940 nm (10–50 mW) for GCaMP and 1100 nm for 647–nm labeled antibody (10–20 mW). The field of view determined the imaging dimensions, for example, 450X450 and 550X550 μm for mouse #2 and #3, respectively (Figure 4). For two-photon cell registration with IHC, we found that to observe stained cells imaging with a longer wavelength was more efficient from the exposed tissue side. In addition, two-photon imaging with two different wavelengths shows chromatic aberrations. Therefore, autofluorescence markers were identified in the images at both wavelengths, and translation in XYZ was applied if needed (up to 25 μm). Images were analyzed in ImageJ, MATLAB, and/or Imaris (Bitplane).

QUANTIFICATION AND STATISTICAL ANALYSIS

MATLAB R2020b was used for statistical analysis. All the statistical details of experiments can be found in the figure legends and in the Results. In all the experiments n represents number of mice, unless assign otherwise. To compares the distributions of two datasets Two-sample Kolmogorov-Smirnov test was used (Figure 3; p represents the null hypothesis that GFP and GFAP expression data are from the same continuous distribution). When the data showed non-normal distribution or biased variation, statistical significance was determined by Kruskal-Wallis test (Figures 6 and S6, n represents number of neurons). All original code has been deposited at Zenodo and is publicly available as of the date of publication. DOI is listed in the Key resources table.

Identifying the target morphology—Axial identification of the target morphology can benefit from a recently published new version of a 3D atlas (Wang et al., 2020) that allows for more straightforward navigation in the mouse brain, including in horizontal planes, and allows for the identification of brain structures at any angle.

Fiber photometry—In all FP experiments, the mean value of dF/F is presented (Figures 2 and S2; SEM-thin black line). The peak area of SCN^{VIP} dF/F was calculated by integrating dF/F from light-on to light-off (15 s) and subtracting the 15–second dark baseline activity (Figure S2B).

To visualize the change in coordinates, ML, AP, and DV coordinates were represented asa distance error, which is the size of the vector from the actual to the final coordinates, defined as $distance\ error = \sqrt{(AP_{final} - AP)^2 + (ML_{final} - ML)^2 + (DL_{final} - DV)^2}$. Initial coordinates: AP: −0.5, ML: 1.17, DV: −5.65mm from brain surface. Finalized: AP: −0.18 (L) and −0.33 (R) an averaged AP value was taken for the calculation, ML: 1.19, DV: −5.5 from the brain surface. All in 13 degrees. The success rate in each session was defined as $100 \cdot (\#animals\ with\ signal = \#animals\ implanted)$ (Figure 2SC).

Reward consumption—In addition to the single trial presentation of the lick activity, the mean value over 21 trials is presented (Figure S2E; thick black - mean, thin black line - SEM).

Fluorescence image quantification—Samples for GFAP labeling were perfused three to six months after implantation. Z stack images were taken with a Zeiss confocal microscope at 10 μm steps, with the 488 nm channel for GFP/GCaMP and the 555 nm channel for GFAP/Alexa Fluor 555, under the same conditions for all samples. Images were quantified by the sum over pixels based on a 450 × 450 μm rectangle around the SCN from each hemisphere, over all-optical sections which had GFP or GCaMP expression, for each channel separately. To compare GFP and GFAP expressions, the fluorescence was normalized to the total fluorescence intensity above both SCN ($RF = I_{implant} = (I_{implant} + I_{no\ implant})$), where $RF = 0{:}5$ represent equal intensity. To compare intact and OVX females, mean values were normalized to the maximum value from all samples and defined as “normalized fluorescence.” The averaged value from both hemispheres was used. In this experiment, VIP x GCaMP6s mice and VIP x GFP mice were used equivalently to visualize VIP neurons (Figure 3).

The SCN-to-fiber distance (z), determined by confocal imaging, was defined as the length of the vector between the fiber inner tip center and the center of the closest SCN (right or left). Fiber tip was identified based on a low autofluorescence background (Imaris, “Surface”).

Cell counting—Images were processed in Imaris: image contrast was normalized by layer. The fiber was defined manually as a surface and was defined as a new channel with distance transformation. Cells were defined with the Imaris wizard (“spots,” 20 μm diameter). The distance reported is the median of distances from cells to the newly defined channel.

Two-photon signal processing—Each transient two-photon imaging session was first corrected for motion artifacts via non-rigid motion correction on a grid of 24 × 24 pixels (NormCorre MATLAB package), then images were averaged and used for further registration. Where temporal data was used (Figure 6), the recordings were analyzed with the suite2P pipeline (Pachitariu et al., 2017), using the sparse mode (Python version, no overlap, tau = 1.25, fs = 4). To register multiple days’ recordings, cell projection images were registered with a geometric transformation (“cpselect” and “fitgeotrans” function, using the “NonreflectiveSimilarity” option, MATLAB) and were analyzed together in Suite2P. Suite2P documentation recommends analyzing consecutive days by saving consecutive .tif files into one folder. All the .tif files in the folder will be analyzed together.

Changes in fluorescence were calculated as $F = F - 0.7 \cdot neuropil$ (where "neuropil" is as defined in suite2P), and $dF = F - median(F)/mad(F)$ (where "mad" is the median absolute deviation). The Z-scored dF was used for event analysis and image maps displaying the normalized Z-scores. Calcium event analysis was carried out with a peak analysis function ("findpeaks," MATLAB).

Two-photon registration pipeline—A pipeline was developed to register three volumes: 1. *in vivo* average recording, 2. fixed tissue through the GRIN lens, and 3. fixed tissue through the tissue side. The pipeline was developed on a cohort of C57 mice injected with AAV1.hSyn.jGCaMP7b or AAV9.hSyn.GCaMP6s and implanted with a 500 μm or 600 μm GRIN lens (n = 6). For two-photon registration, the volume beneath each mounted fixed sample was imaged using a two-photon microscope at 940 nm through the GRIN lens and at the tissue side in 5 μm steps. Sample orientation was matched between *ex vivo* and *in vivo* imaging sessions. The volumes were inspected in ImageJ to conduct point set registration. After manual inspection of the three volumes, three to seven control point pairs per slice were used to build the geometric transformation while keeping the fixed-tissue section obtained through the GRIN lens as an anchor (Figures 4B and 4C), with the other slices registered to it. The registration process was conducted in MATLAB using "cpselect" and "fitgeotrans" functions ("NonreflectiveSimilarity" option). All registrations were first determined for each optical section separately, using linear transformation (by angle and scale). Magnification was defined as 1/scale. The transformation was followed by a non-rigid registration step ('imregdemons, MATLAB, which estimate displacement field that aligns two 2-D or 3-D images, using 'AccumulatedFieldSmoothing ' = 1.5 and 'PyramidLevels' = 1), which slightly improved the image similarity score (SSIM, MATLAB, by 1.2 ± 0.4%). The volumetric transformation matrix (Figure 4D) included only the relative angle and scale. It was constructed by independently registering five optical sections and then averaging the angle, while the scale was interpolated over a 75 μm depth.

To assess how many cells were identified in the fixed tissue relative to the mean *in vivo* planes, cells were manually selected from the mean *in vivo* image. Only cells for which the mean intensity value of the center was three standard deviations above the mean value of the whole image were counted as cells, and an ROI was defined as a fixed square around them. Verified cells were compared to the same ROI using the MATLAB "ssim" function, setting the "Exponents" vector to [0.8 0.8 0.8].

Two-photon registration with staining—For staining, a secondary 647-nm antibody was used, and this channel was imaged using a two-photon or a confocal microscope. Additional secondary antibody was imaged using a confocal microscope, such as 555-nm. When using a two-photon microscope, imaging was conducted both through the GRIN lens and from the exposed tissue side for each wavelength. We used laser excitation at 1100 nm for Alexa Fluor 647, which does not overlap with the two-photon excitation-emission spectra of GCaMP (Mütze et al., 2012). The two wavelength excitation z stacks were inspected, and slight translations between the channels due to chromatic aberrations were corrected (Figure 5). The three acquired volumes were registered in the same way as

described above, and the transformation matrix from the GCaMP channel was applied to the stained images as well.

For antibody-labeled cell identification and visualization, the stained channel imaged from the exposed tissue side was used. We found that the two-photon microscope produced better images through the GRIN lens than the confocal microscope. However, for registering the stained channels, it is possible to use a confocal microscope to image two (or more) channels simultaneously from the exposed tissue side and register directly from the *in vivo* images to the fixed, tissue-side z stack images. The Airyscan option can improve the S/N ratio and was used in Figures 6 and S6. In this case, an optical section of 30 μm was used.

Following the suite2P pipeline for GCaMP analysis, the contour map of all active cells was overlaid with the stained image. Next, overlaid cells were identified. For comparison purposes, a similar number of non-stained cells was selected as well. Event analysis was performed again on the identified subpopulations.

Supplementary Material

Refer to Web version on PubMed Central for supplementary material.

ACKNOWLEDGMENTS

We would like to thank the Gradinaru laboratory and Prof. Justin Bois for helpful discussions, the Caltech Neurotechnology Laboratory for the two-photon microscope support, the Caltech Biological Imaging Center for the training and use of the Airyscan confocal microscope, and Dr. Ariane Helou for editorial comments. Professor Gradinaru is a Heritage Principal Investigator supported by the Heritage Medical Research Institute; this work was also funded by the NIH Director's New Innovator IDP20D017782–01, the NSF NeuroNex Technology Hub 1707316, Presidential Early Career Awards for Scientists and Engineers (V.G.), NIH Brain Research through Advancing Innovative Neurotechnologies RF1MH117069, and the Beckman Institute's Resource Center on CLARITY, Optogenetics, and Vector Engineering (CLOVER). We would also like to thank CLOVER for technology development and broad dissemination (https://beckmaninstitute.caltech.edu/clover.shtml). A.K. is supported by a Caltech Biology and Biological Engineering department postdoctoral fellowship and the Hebrew University Postdoctoral Fellowship for Women, Israel. A.G. is a Good Ventures Fellow of the Life Sciences Research Foundation. P.K. is supported by the Swiss National Science Foundation (P2EZP3–181896).

REFERENCES

Abdelfattah AS, Kawashima T, Singh A, Novak O, Liu H, Shuai Y, Huang Y-C, Campagnola L, Seeman SC, Yu J., et al. (2019). Bright and photostable chemigenetic indicators for extended in vivo voltage imaging. Science 365, 699–704. [PubMed: 31371562]

Anner P, Passecker J, Klausberger T, and Dorffner G. (2020). Ca^{2+} imaging of neurons in freely moving rats with automatic post hoc histological identification. J. Neurosci. Methods 341, 108765. [PubMed: 32407804]

Biran I, Yu X, and Walt DR (2008). Optrode-based fiber optic biosensors (bio-optrode). In Optical Biosensors, Second Edition, Ligler FS and Taitt CR, eds. (Elsevier), pp. 3–82.

Campbell A, and Wu C. (2018). Chronically Implanted Intracranial Electrodes: Tissue Reaction and Electrical Changes. Micromachines (Basel) 9, 430.

Cetin A, Komai S, Eliava M, Seeburg PH, and Osten P. (2006). Stereotaxic gene delivery in the rodent brain. Nat. Protoc 1, 3166–3173. [PubMed: 17406580]

Cho JR, Treweek JB, Robinson JE, Xiao C, Bremner LR, Greenbaum A, and Gradinaru V. (2017). Dorsal raphe dopamine neurons modulate arousal and promote wakefulness by salient stimuli. Neuron 94, 1205–1219.e8. [PubMed: 28602690]

Choi HMT, Beck VA, and Pierce NA (2014). Next-generation in situ hybridization chain reaction: higher gain, lower cost, greater durability. ACS Nano 8, 4284–4294. [PubMed: 24712299]

Fenno L, Yizhar O, and Deisseroth K. (2011). The development and application of optogenetics. Annu. Rev. Neurosci 34, 389–412. [PubMed: 21692661]

Fernandez DC, Komal R, Langel J, Ma J, Duy PQ, Penzo MA, Zhao H, and Hattar S. (2020). Retinal innervation tunes circuits that drive nonphotic entrainment to food. Nature 581, 194–198. [PubMed: 32404998]

Franklin K, and Paxinos G. (2004). Paxinos and Franklin's The Mouse Brain in Stereotaxic Coordinates, Fifth Edition (Harvard).

Goldey GJ, Roumis DK, Glickfeld LL, Kerlin AM, Reid RC, Bonin V, Schafer DP, and Andermann ML (2014). Removable cranial windows for long-term imaging in awake mice. Nat. Protoc 9, 2515–2538. [PubMed: 25275789]

Gouwens NW, Sorensen SA, Berg J, Lee C, Jarsky T, Ting J, Sunkin SM, Feng D, Anastassiou CA, Barkan E., et al. (2019). Classification of electrophysiological and morphological neuron types in the mouse visual cortex. Nat. Neurosci 22, 1182–1195. [PubMed: 31209381]

Gunaydin LA, Grosenick L, Finkelstein JC, Kauvar IV, Fenno LE, Adhikari A, Lammel S, Mirzabekov JJ, Airan RD, Zalocusky KA, et al. (2014). Natural neural projection dynamics underlying social behavior. Cell 157, 1535–1551. [PubMed: 24949967]

Guo D, Zou J, Rensing N, and Wong M. (2017). In vivo two-photon imaging of astrocytes in GFAP-GFP transgenic mice. PLoS One 12, e0170005. [PubMed: 28107381]

Guzowski JF, Timlin JA, Roysam B, McNaughton BL, Worley PF, and Barnes CA (2005). Mapping behaviorally relevant neural circuits with immediate–early gene expression. Curr. Opin. Neurobiol 15, 599–606. [PubMed: 16150584]

Holtmaat A, Bonhoeffer T, Chow DK, Chuckowree J, De Paola V, Hofer SB, Hübener M, Keck T, Knott G, Lee W-CA, et al. (2009). Long-term, high-resolution imaging in the mouse neocortex through a chronic cranial window. Nat. Protoc 4, 1128–1144. [PubMed: 19617885]

Jennings JH, Kim CK, Marshel JH, Raffiee M, Ye L, Quirin S, Pak S, Ramakrishnan C, and Deisseroth K. (2019). Interacting neural ensembles in orbitofrontal cortex for social and feeding behaviour. Nature 565, 645–649. [PubMed: 30651638]

Jones JR, Tackenberg MC, and McMahon DG (2015). Manipulating circadian clock neuron firing rate resets molecular circadian rhythms and behavior. Nat. Neurosci 18, 373–375. [PubMed: 25643294]

Jones JR, Simon T, Lones L, and Herzog ED (2018). SCN VIP neurons are essential for normal light-mediated resetting of the circadian system. J. Neurosci 38, 7986–7995. [PubMed: 30082421]

Ke M-T, Fujimoto S, and Imai T. (2013). SeeDB: a simple and morphology-preserving optical clearing agent for neuronal circuit reconstruction. Nat. Neurosci 16, 1154–1161. [PubMed: 23792946]

Keller AJ, and Martin KAC (2015). Local circuits for contrast normalization and adaptation investigated with two-photon imaging in cat primary visual cortex. J. Neurosci 35, 10078–10087. [PubMed: 26157005]

Khan AG, Poort J, Chadwick A, Blot A, Sahani M, Mrsic-Flogel TD, and Hofer SB (2018). Distinct learning-induced changes in stimulus selectivity and interactions of GABAergic interneuron classes in visual cortex. Nat. Neurosci 21, 851–859. [PubMed: 29786081]

Kim CK, Yang SJ, Pichamoorthy N, Young NP, Kauvar I, Jennings JH, Lerner TN, Berndt A, Lee SY, Ramakrishnan C., et al. (2016). Simultaneous fast measurement of circuit dynamics at multiple sites across the mammalian brain. Nat. Methods 13, 325–328. [PubMed: 26878381]

Langer D, and Helmchen F. (2012). Post hoc immunostaining of GABAergic neuronal subtypes following in vivo two-photon calcium imaging in mouse neocortex. Pflugers Arch 463, 339–354. [PubMed: 22134770]

Lerner TN, Shilyansky C, Davidson TJ, Evans KE, Beier KT, Zalocusky KA, Crow AK, Malenka RC, Luo L, Tomer R, and Deisseroth K. (2015). Intact-brain analyses reveal distinct information carried by SNc dopamine subcircuits. Cell 162, 635–647. [PubMed: 26232229]

Li C, White AC, Schochet T, McGinty JF, and Frantz KJ (2018). ARC and BDNF expression after cocaine self-administration or cue-induced reinstatement of cocaine seeking in adolescent and adult male rats. Addict. Biol 23, 1233–1241. [PubMed: 30421552]

Lin R, Wang R, Yuan J, Feng Q, Zhou Y, Zeng S, Ren M, Jiang S, Ni H, Zhou C., et al. (2018). Cell-type-specific and projection-specific brain-wide reconstruction of single neurons. Nat. Methods 15, 1033–1036. [PubMed: 30455464]

Losi G, Mariotti L, Sessolo M, and Carmignoto G. (2017). New tools to study astrocyte Ca2+ signal dynamics in brain networks in vivo. Front. Cell. Neurosci 11, 134. [PubMed: 28536505]

Lovett-Barron M, Chen R, Bradbury S, Andalman AS, Wagle M, Guo S, and Deisseroth K. (2020). Multiple convergent hypothalamus-brainstem circuits drive defensive behavior. Nat. Neurosci 23, 959–967. [PubMed: 32572237]

Lu R, Sun W, Liang Y, Kerlin A, Bierfeld J, Seelig JD, Wilson DE, Scholl B, Mohar B, Tanimoto M., et al. (2017). Video-rate volumetric functional imaging of the brain at synaptic resolution. Nat. Neurosci 20, 620–628. [PubMed: 28250408]

Luo Z, Volkow ND, Heintz N, Pan Y, and Du C. (2011). Acute cocaine induces fast activation of D1 receptor and progressive deactivation of D2 receptor striatal neurons: in vivo optical microprobe [Ca2+]i imaging. J. Neurosci 31, 13180–13190. [PubMed: 21917801]

Ma Y, Guo H, Zhang L, Tao L, Yin A, Liu Z, Li Y, Dong H, Xiong L, and Hou W. (2016). Estrogen replacement therapy-induced neuroprotection against brain ischemia-reperfusion injury involves the activation of astrocytes via estrogen receptor b. Sci. Rep 6, 21467. [PubMed: 26891996]

Mazuski C, Abel JH, Chen SP, Hermanstyne TO, Jones JR, Simon T, Doyle FJ 3rd, and Herzog ED (2018). Entrainment of circadian rhythms depends on firing rates and neuropeptide release of VIP SCN neurons. Neuron 99, 555–563.e5. [PubMed: 30017392]

Mei L, Fan Y, Lv X, Welsh DK, Zhan C, and Zhang EE (2018). Long-term in vivo recording of circadian rhythms in brains of freely moving mice. Proc. Natl. Acad. Sci. USA 115, 4276–4281. [PubMed: 29610316]

Meng G, Liang Y, Sarsfield S, Jiang W-C, Lu R, Dudman JT, Aponte Y, and Ji N. (2019). High-throughput synapse-resolving two-photon fluorescence microendoscopy for deep-brain volumetric imaging in vivo. eLife 8, e40805. [PubMed: 30604680]

Mütze J, Iyer V, Macklin JJ, Colonell J, Karsh B, Petrášek Z, Schwille P, Looger LL, Lavis LD, and Harris TD (2012). Excitation spectra and brightness optimization of two-photon excited probes. Biophys. J 102, 934–944. [PubMed: 22385865]

Pachitariu M, Stringer C, Dipoppa M, Schröder S, Rossi LF, Dalgleish H, Carandini M, and Harris KD (2017). Suite2p: beyond 10,000 neurons with standard two-photon microscopy. bioRxiv.

Park S, Guo Y, Jia X, Choe HK, Grena B, Kang J, Park J, Lu C, Canales A, Chen R., et al. (2017). One-step optogenetics with multifunctional flexible polymer fibers. Nat. Neurosci 20, 612–619. [PubMed: 28218915]

Patel AA, McAlinden N, Mathieson K, and Sakata S. (2020). Simultaneous electrophysiology and fiber photometry in freely behaving mice. Front. Neurosci 14, 148. [PubMed: 32153363]

Patriarchi T, Cho JR, Merten K, Howe MW, Marley A, Xiong W-H, Folk RW, Broussard GJ, Liang R, Jang MJ, et al. (2018). Ultrafast neuronal imaging of dopamine dynamics with designed genetically encoded sensors. Science 360, eaat4422. [PubMed: 29853555]

Pflüger P, Pinnell RC, Martini N, and Hofmann UG (2020). Chronically implanted microelectrodes cause *c-fos* expression along their trajectory. Front. Neurosci 13, 1367. [PubMed: 31998057]

Piatkevich KD, Jung EE, Straub C, Linghu C, Park D, Suk H-J, Hochbaum DR, Goodwin D, Pnevmatikakis E, Pak N., et al. (2018). A robotic multidimensional directed evolution approach applied to fluorescent voltage reporters. Nat. Chem. Biol 14, 352–360. [PubMed: 29483642]

Renier N, Wu Z, Simon DJ, Yang J, Ariel P, and Tessier-Lavigne M. (2014). iDISCO: a simple, rapid method to immunolabel large tissue samples for volume imaging. Cell 159, 896–910. [PubMed: 25417164]

Sofroniew MV, and Vinters HV (2010). Astrocytes: biology and pathology. Acta Neuropathol. 119, 7–35. [PubMed: 20012068]

Sych Y, Chernysheva M, Sumanovski LT, and Helmchen F. (2019). High-density multi-fiber photometry for studying large-scale brain circuit dynamics. Nat. Methods 16, 553–560. [PubMed: 31086339]

Tan A, Moratalla R, Lyford GL, Worley P, and Graybiel AM (2000). The activity-regulated cytoskeletal-associated protein arc is expressed in different striosome-matrix patterns following exposure to amphetamine and cocaine. J. Neurochem 74, 2074–2078. [PubMed: 10800951]

Ueda HR, Ertürk A, Chung K, Gradinaru V, Chédotal A, Tomancak P, and Keller PJ (2020). Tissue clearing and its applications in neuroscience. Nat. Rev. Neurosci 21, 61–79. [PubMed: 31896771]

Vassilev P, Avvisati R, Koya E, and Badiani A. (2020). Distinct populations of neurons activated by heroin and cocaine in the striatum as assessed by cat-FISH. eNeuro 7, ENEURO.0394–19.2019.

von Buchholtz LJ, Ghitani N, Lam RM, Licholai JA, Chesler AT, and Ryba NJP (2021). Decoding cellular mechanisms for mechanosensory discrimination. Neuron 109, 285–298.e5. [PubMed: 33186546]

Wang Q, Ding S-L, Li Y, Royall J, Feng D, Lesnar P, Graddis N, Naeemi M, Facer B, Ho A., et al. (2020). The Allen Mouse Brain Common Coordinate Framework: a 3D reference atlas. Cell 181, 936–953.e20. [PubMed: 32386544]

Wilson DE, Smith GB, Jacob AL, Walker T, Dimidschstein J, Fishell G, and Fitzpatrick D. (2017). GABAergic neurons in ferret visual cortex participate in functionally specific networks. Neuron 93, 1058–1065.e4. [PubMed: 28279352]

Xie Y, Martini N, Hassler C, Kirch RD, Stieglitz T, Seifert A, and Hofmann UG (2014). In vivo monitoring of glial scar proliferation on chronically implanted neural electrodes by fiber optical coherence tomography. Front. Neuroeng 7, 34. [PubMed: 25191264]

Xu S, Yang H, Menon V, Lemire AL, Wang L, Henry FE, Turaga SC, and Sternson SM (2020). Behavioral state coding by molecularly defined paraventricular hypothalamic cell type ensembles. Science 370, eabb2494. [PubMed: 33060330]

Yizhar O, Fenno LE, Davidson TJ, Mogri M, and Deisseroth K. (2011). Optogenetics in neural systems. Neuron 71, 9–34. [PubMed: 21745635]

Young A. (2018). Arduino light sensor using a photoresistor (Pi My Life Up), Published online November 2, 2018. Updated November 17, 2019. https://pimylifeup.com/arduino-light-sensor/.

Zou P, Zhao Y, Douglass AD, Hochbaum DR, Brinks D, Werley CA, Harrison DJ, Campbell RE, and Cohen AE (2014). Bright and fast multi-coloured voltage reporters via electrochromic FRET. Nat. Commun 5, 4625. [PubMed: 25118186]

Highlights

- LiGS provides precise optical implant localization and surrounding tissue analysis
- Optical fiber positioning errors are correlated with calcium signal strength
- Glial scar formation around the optical implant is visualized in the brain
- Post hoc cell registration with two-photon calcium imaging and molecular features

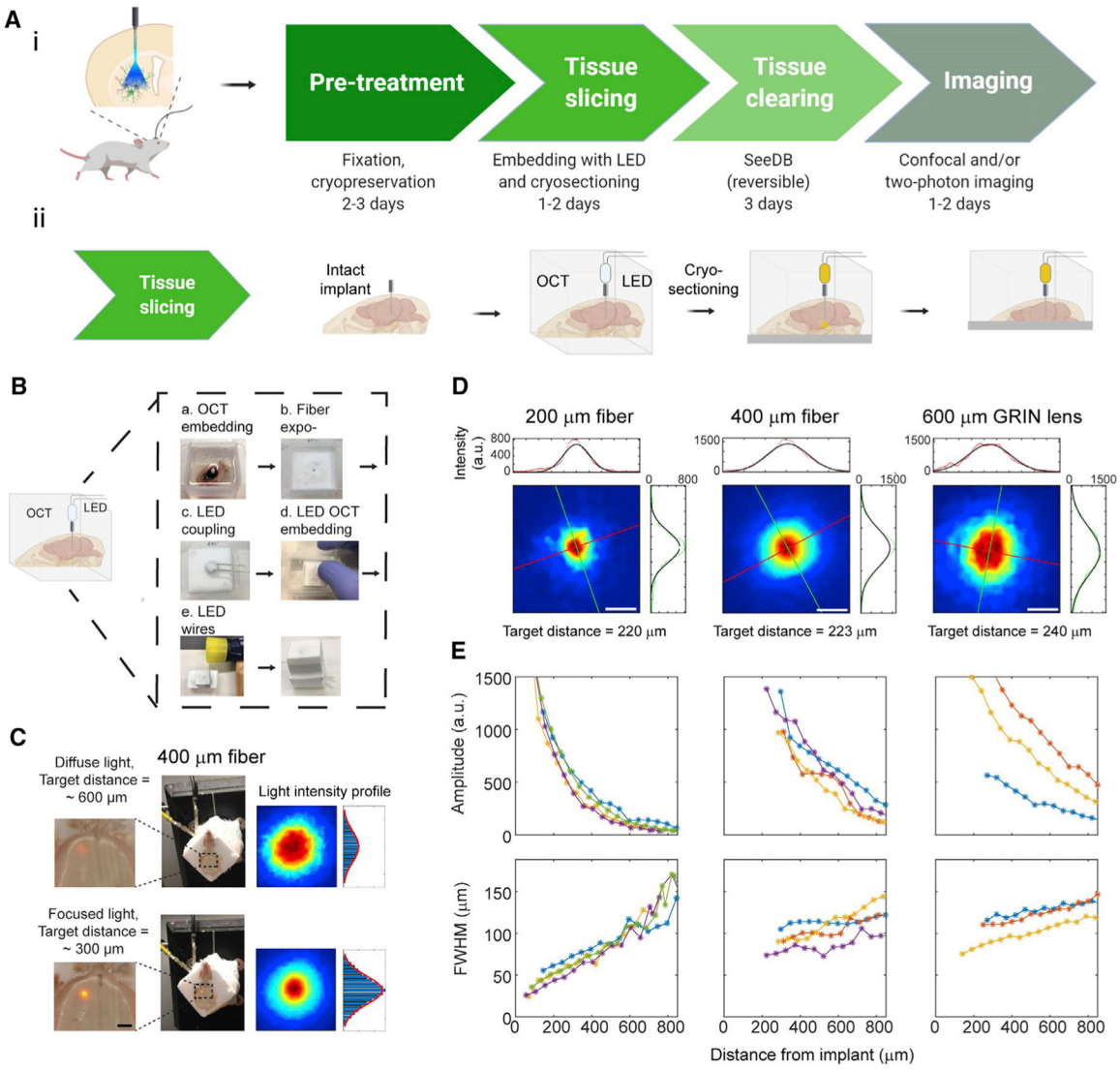

Figure 1. Light-guided sectioning (LiGS) method for *in situ* visualizations of optical implants

(A) LiGS basic pipeline (i): a pre-treatment step is performed (fixation, cryopreservation), followed by tissue slicing (ii) after the sample is embedded in OCT with an LED, tissue clearing, and imaging.

(B) A detailed demonstration of coupling a sample to an LED with OCT. (a) Embedding the sample in OCT. (b) The OCT should not cover the optical implant; if it does, the OCT can be gently removed. (c) A 5-mm LED is placed above the optical device with an additional OCT. (d) A second embedding mold is half filled with OCT, and the brain is placed upside down. (e) The LED wires are exposed.

(C) The implant-surface distance is estimated from the light pattern emitted by the LED, which propagates through the implant and the tissue, as shown at a depth of ~600 μm (top row, wide pattern with low amplitude) and ~300 μm (bottom row, narrow pattern with high amplitude).

(D) Representative images of light patterns generated by various optical implants (200, 400, and 600 μm diameter) at similar target distances (220–240 μm). Fitted two-dimensional (2D) Gaussian profiles of the diffused light for the various optical implants are shown as well. (E) The amplitude and the full-width half maximum of the fitted Gaussian were plotted against the distance from the implant (200, 400, and 600 μm diameter, n = 4, 4, and 3, respectively) Scale bars represent 2 mm (C) and 100 μm (D).

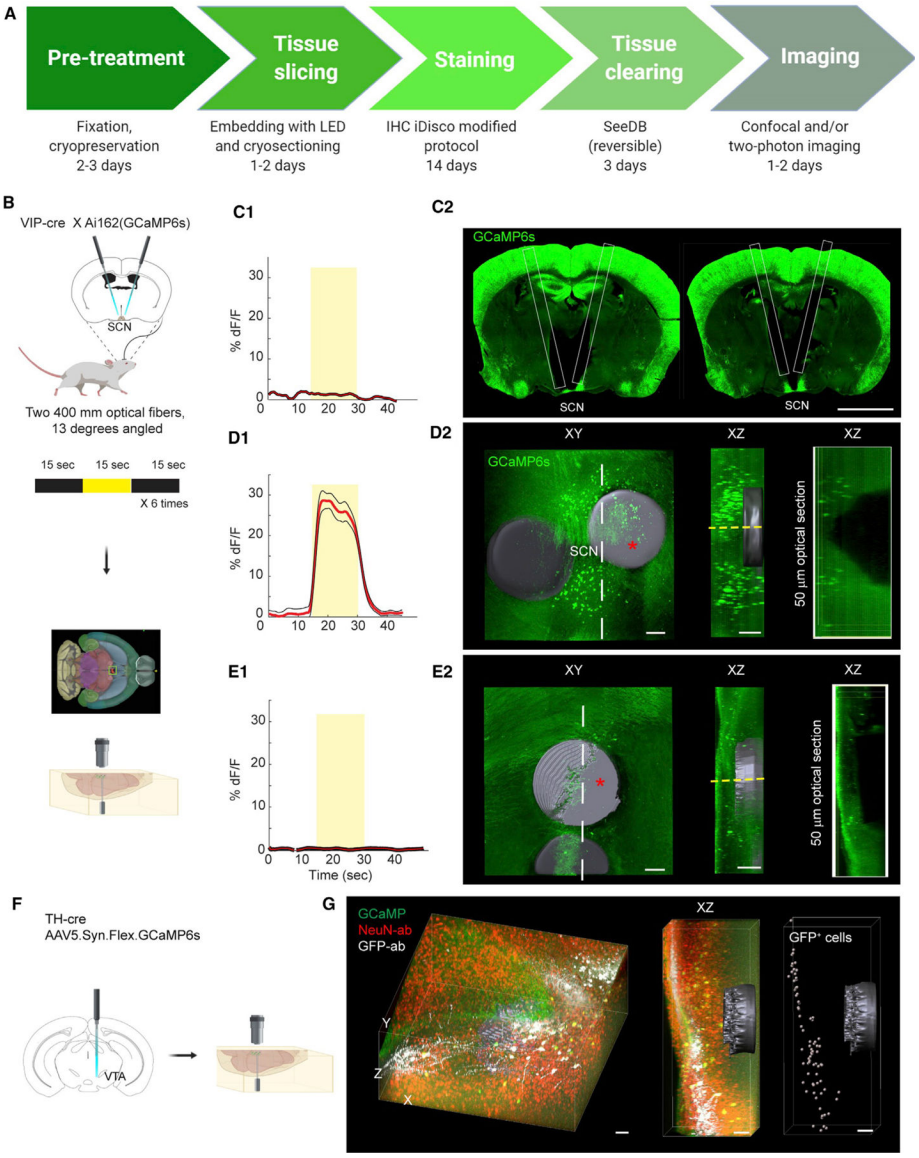

Figure 2. Identifying cell population at the volume below the implant using LiGS and IHC

(A) To the basic pipeline in Figure 1, a staining step is added.

(B) Experimental scheme: VIP × GCaMP6s mice were implanted with two optical fibers targeting the SCN. After *in vivo* recording of SCN^{VIP} FP dF/F response, LiGS histology was performed, and the processed tissue was imaged.

(C) An example of minor FP response to ambient room light exposure (1). The 2D coronal histology (2) corresponds to that in (1). The fibers' locations were estimated from the fiber tracks (white).

(D and E) SCN^{VIP} FP dF/F response to ambient room light exposure (red, mean dF/F; black, SEM; six repeats) (D, 2). LiGS histology for the two mice shown in (D), 1 and (E), 1, respectively, and in (E), 2. The recorded implant location is marked with a red asterisk. Left and middle: MIP images, projected onto the xy and xz planes. Optical fiber surface (gray),

fiber orientation progression (yellow dashed line), and GCaMP stained with GFP-ab (green). Right: a single digital section in the xz plane (5 μm thickness).
(F) A Th-cre mouse expressing GCaMP6s was implanted with an optical fiber (400 μm diameter) in the VTA, followed by LiGS histology.
(G) A 3D reconstruction of the fiber-tissue interface: virus expression (green), cell labeling for GCaMP (GFP-ab, white), neurons (NeuN-ab, red), and optical fiber location (gray, based on low autofluorescence). Middle: an xz view. Right: identified GCaMP-expressing cells (gray circles; Imaris). All fixed-tissue imaging took place from the exposed tissue side.
Scale bars represent 2 mm (C, 2), and 100 μm (D, 2; E, 2; and G).

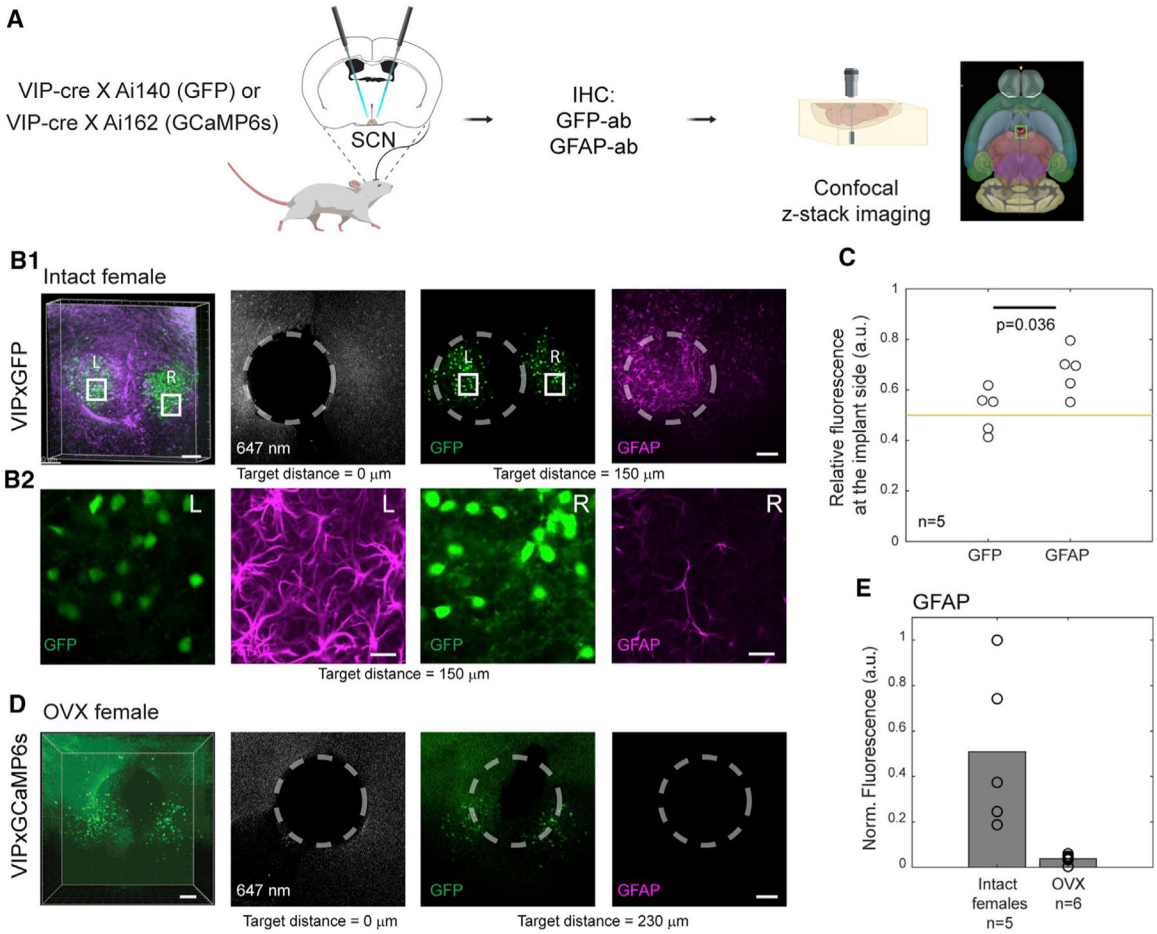

Figure 3. Investigating the effect of implants on the surrounding volume using LiGS and IHC

(A) VIP × GFP or VIP × GCaMP6s mice were implanted with one or two optical fibers targeting the SCN. Tissue processing included IHC labeling for GFP and GFAP.

(B) Representative images from an intact female. (1) From left to right: 3D view of the SCN and fiber, fiber location imaged with a 647-nm channel (gray), GFP expression (green), and GFAP-ab labeling (magenta). (2) Magnified images of the white squares in (1) (L, left; R, right), showing GFP and GFAP-ab expression.

(C) The RF of the implanted side in GFP versus GFAP. The RF of GFP is around 0.5 (equal distribution); the distribution of the RF of GFAP is greater toward the implant side. ($p = 0.036$, two-sample Kolmogorov-Smirnov test; $n = 5$, 3 females, 2 males).

(D) Representative images from an OVX female. From left to right: 3D view of the SCN, fiber (gray, based on low autofluorescence), GFP expression (green), and GFAP-ab staining (magenta).

(E) The overall integrated GFAP fluorescence from the SCN of intact versus OVX females (bars, mean values; circles, individual values). GFAP-ab expression in females decreases from 0.77 in intact females to 0.05 in OVX ($n_{intact} = 5$, $n_{OVX} = 6$). All images were taken under the same conditions in a confocal microscope with matched brightness and contrast. "Target distance" is the relative distance from the fiber surface (target distance = 0) to the

optical section in interest. Dashed circles indicate the implant location. Dashed circles are used to indicate the fiber tip location.

Scale bars represent 100 μm (B, 1; and D) and 20 μm (B, 2).

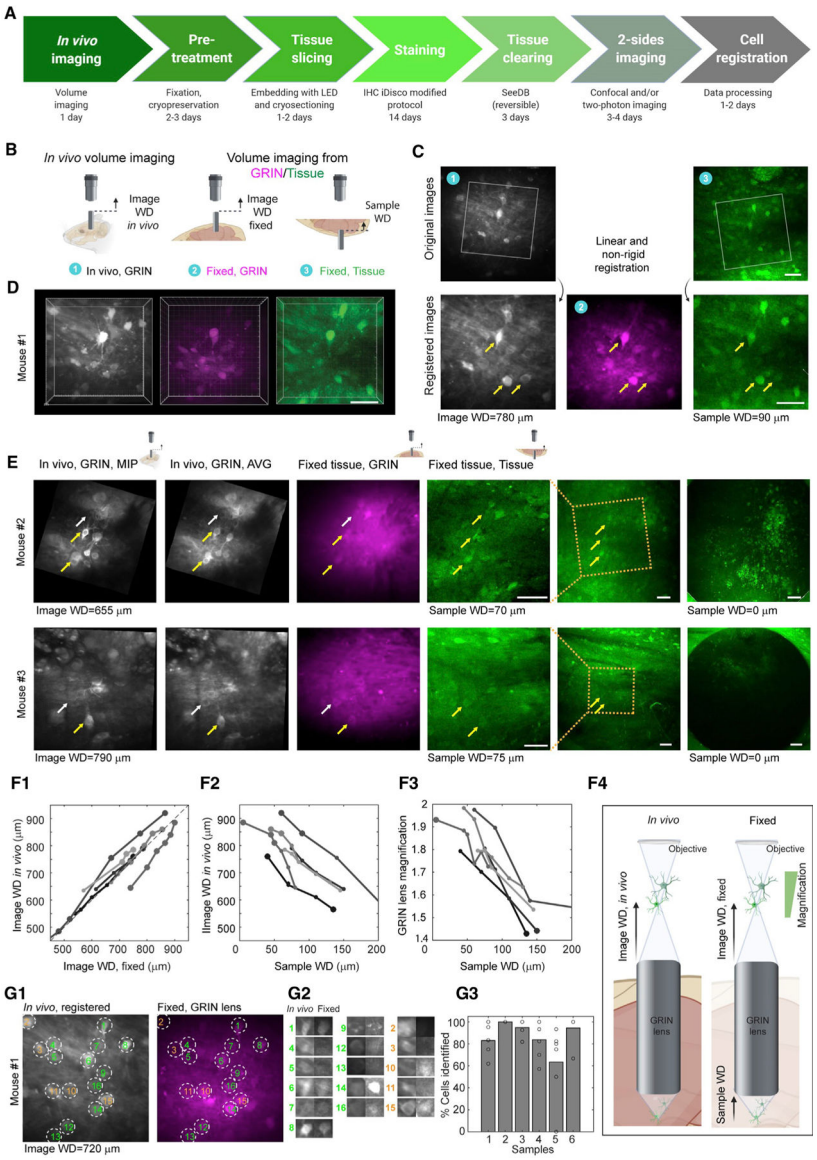

Figure 4. Two-photon cell registration using imaging through the GRIN lens as an intermediate step

(A) Additional steps were added to the pipeline: *in vivo* z stack, imaging from both sides of the sample, i.e., through the GRIN lens and the exposed tissue side, and a cell-registration step.

(B) Imaging and single-cell-resolution registration pipeline: (Left) *in vivo* volume imaging. (Middle) *ex vivo* volume imaging through the GRIN lens. (Right) z stack optical sections taken through the tissue side.

(C) An example of cell registration in one optical section. Left: an AVG of *in vivo* recording (gray); the original image (top); the registered image after non-rigid transformation (bottom). Middle: fixed-tissue volume, imaged through the intact GRIN lens (purple). Right: the equivalent ROIs taken from the tissue side, the original image (upper), and the registered image (bottom). Yellow arrows indicate neurons that were used as landmarks.

(D). A 3D reconstruction of the sample in (C).

(E) *In vivo* MIPs and AVG (gray) registered to the fixed-tissue images taken through the GRIN lens (magenta). White arrows indicate neurons that can be better observed using the AVG images. Three images from the exposed tissue side (green): from left to right, the registered image, the original image, and the relative GRIN lens surface. The GRIN lens edges can be seen at the corners of the right images. Green: the small FOV compared with the GRIN lens diameter and the FOV locations (n = 2).
(F) Comparing the image WD determined *in vivo* and the image WD determined in fixed tissue, both imaged through the GRIN lens (1). Image WD compared with sample WD (2). GRIN lens magnification factor as a function of the sample's WD (3). Summary of the conclusions from the registration process (4), which arise based on (1)–(3).
(G) Quantification of the registration. (1) A comparison between an *in vivo* AVG image and a fixed-tissue image from mouse 1, both taken through the GRIN lens at an image WD of 720 μm. Cell images with an SSIM score greater or less than 0.5 are marked in green or orange, respectively. (2) A closer look at the cells identified in (1). (3) The number of cells identified in fixed tissue as a percentage of those identified *in vivo*, based on the SSIM score (bars represent means over optical sections in each brain sample, n = 6).
Scale bars are given only for images taken through the tissue side because imaging through the GRIN lens causes magnification. Scale bars, 50 μm.

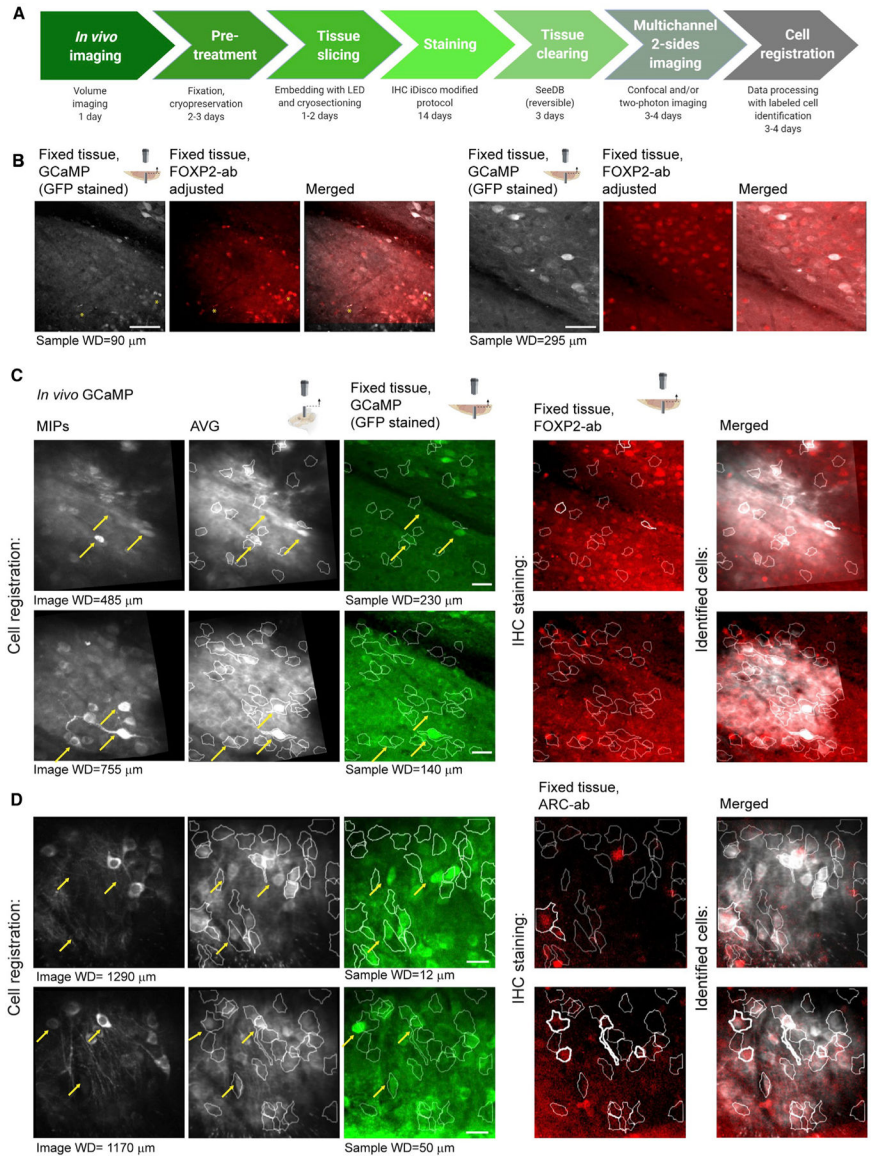

Figure 5. Two-photon cell registration with subpopulation labeling

(A) After *in vivo* experiments with a GRIN lens, LiGS histology is performed. A methanol-free iDISCO protocol for IHC is used, followed by the SeeDB protocol for clearing, and then, fixed tissue is imaged from the exposed tissue side and through the GRIN lens. After cell registration, the cells that are both GCaMP active and labeled can be identified.

(B) Small translation adjustments were needed because of chromatic aberration when imaging with a second wavelength with a two-photon microscope (FOXP2, red; 1,100 nm excitation). Yellow asterisks: autofluorescence landmarks used for registration (tissue side, sample WD = 90 µm).

(C) Example one: a C57BL/6N male mouse expressing GCaMP7b in the striatum, implanted with a GRIN lens (600 µm diameter). Cell registration is shown at image WDs of 485 and 775 µm, corresponding to sample WDs of 230 and 140 µm, respectively. Gray: *in vivo* MIPs and AVG images (registered). Green: the corresponding GCaMP (GFP stained)

optical section that was imaged from the exposed tissue side (940 nm excitation). Red: corresponding FOXP2 labeling. Right: a FOXP2 labeling image merged with the *in vivo* AVG (gray). White borders: $GCaMP^+/FOXP2^-$ cells; bright white borders: $GCaMP^+/FOXP2^+$ cells.

(D) Example two: C57BL/6N mouse expressing GCaMP6s in the striatum was implanted with a GRIN lens (500 μm diameter). Cell registration is shown at image WDs of 1,290 and 1,170 μm, corresponding to sample WDs of 12 and 50 μm. Gray: MIPs and AVG of *in vivo* recording, registered. Green: the corresponding GCaMP optical section, imaged from the exposed tissue side (488 nm, confocal microscope). Red: corresponding ARC labeling (633 nm excitation). Right: a merged image of the *in vivo* AVG (gray) and ARC-labeled cells (red). White borders: $GCaMP^+/ARC^-$ cells; bright white borders: $GCaMP^+/ARC^+$ cells. The yellow arrows in (C) and (D) indicate neurons used as landmarks for registration. Scale bars, 50 μm.

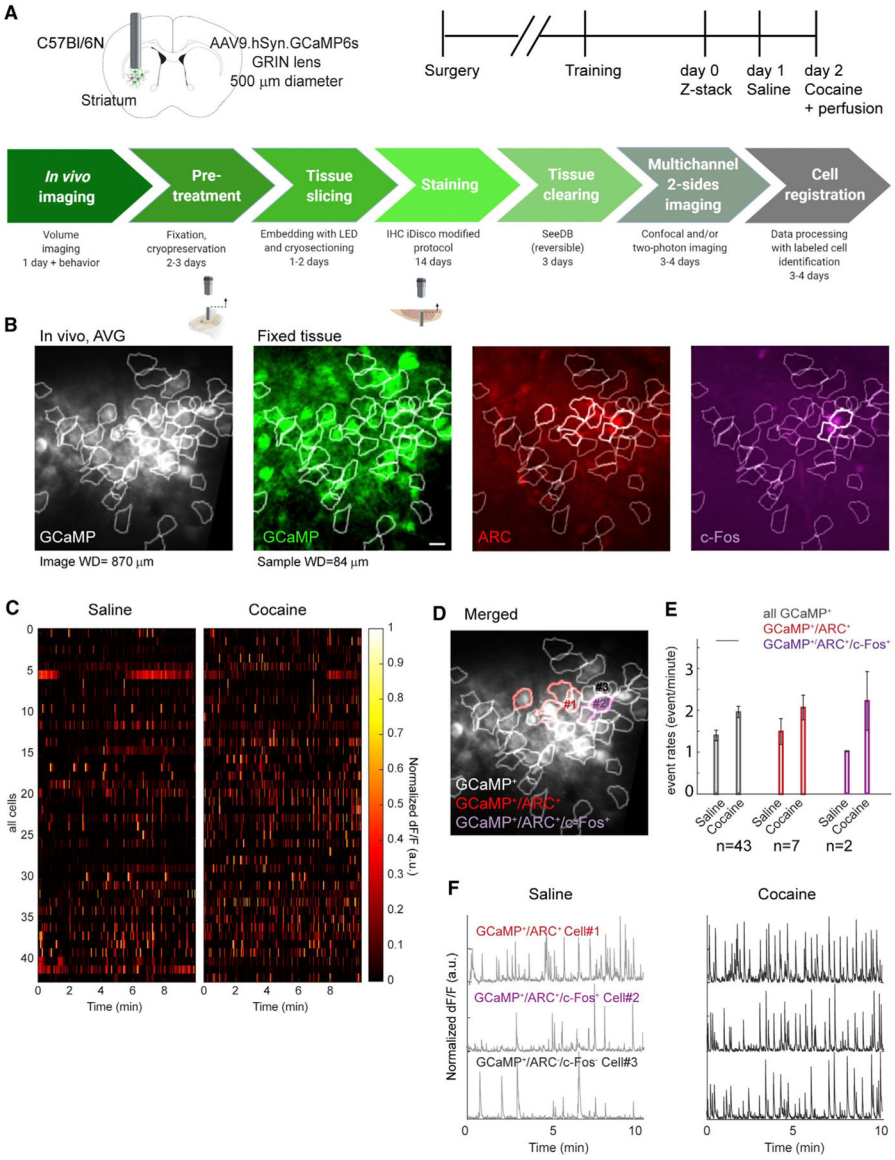

Figure 6. Application of the LiGS method to two-photon GRIN-lens GCaMP imaging to identify and characterize active neurons by ARC and c-Fos

(A) Behavioral experiment setup and the tissue processing pipeline. A C57BL/6N mouse was implanted with a GRIN lens (500 µm diameter) and injected with AAV9.hSyn.GCaMP6s. After habituation for head fixation, volume imaging was performed (day 0). In the following days (days 1 and 2), the mouse was injected with saline and cocaine, respectively, and imaged *in vivo* for 10 min each time at a single optical section (at an image WD of 870 µm).

(B) The *in vivo* AVG image (gray) corresponds to a sample WD of 84 µm with GCaMP signal (green), ARC labeling (red), and c-Fos labeling (purple). Seven neurons were identified as $GCaMP^+/ARC^+$, and two of them were also identified as $c\text{-}Fos^+$ (thick white borders).

(C) Normalized dF/F traces of $GCaMP^+$ neurons after the first saline administration (saline) and after the cocaine administration (cocaine), sorted by mean event rates during the cocaine session.
(D) Merged image of the *in vivo* AVG image with the contours of the $GCaMP^+/ARC^+$ neurons (red) and the $GCaMP^+/ARC^+/c\text{-}Fos^+$ neurons (purple).
(E) Quantification of GCaMP activity, saline versus cocaine administration, showing mean event rates. A comparison of all active neurons (gray), $GCaMP^+/ARC^+$ (red), and $GCaMP^+/ARC^+/c\text{-}Fos^+$ (purple) is shown ($n_{neurons}$ = 43, 7, and 2, respectively. The black line indicates $p < 0.0005$, non-parametric Kruskal-Wallis test. Bars represent means ± SEM).
(F) Examples of dF/F traces of neurons from each of the groups presented in (E).
Scale bars, 20 μm.

KEY RESOURCES TABLE

REAGENT or RESOURCE	SOURCE	IDENTIFIER
Antibodies		
NeuN (Rabbit)	Abcam	Cat# Ab177487; RRID:AB_2532109
GFP (Chicken)	Aves	Cat# GFP-1020; RRID:AB_10000240
FOXP2 (Rabbit)	Abcam	Cat# Ab16046; RRID:AB_2107107
Estrogen receptor 1 (Rabbit)	Millipore	Cat# 06–935; RRID:AB_310305
GFAP (Chicken)	Abcam	Cat# ab4674; RRID:AB_304558
Iba1 (Rabbit)	Fuji Film	Cat# 019–19741; RRID:AB_839504
S100beta (Rabbit)	Abcam	Cat# ab52642; RRID:AB_882426
ARC (Rabbit)	Synaptic Systems	Cat# 156003; RRID:AB_887694
c-Fos (Mouse)	Santa Cruz Biotechnology	Cat# Sc-166940; RRID:AB_10609634
Alexa Fluor 647 AffiniPure Fab Fragment Donkey Anti-Rabbit IgG (H+L)	Jackson Immune	Cat# 711–607-003; RRID:AB_2340626
Goat Anti-Chicken IgY H&L (Alexa Fluor 555)	Abcam	Cat# ab150170
Alexa Fluor 488 AffiniPure F(ab')2 Fragment Donkey Anti-Chicken IgY (IgG) (H+L)	Jackson Immune	Cat# 703–546-155; RRID:AB_2340376
Donkey Anti-Mouse IgG H&L (Alexa Fluor 555)	Abcam	Cat# Ab150106; RRID:AB_2857373
HCR probes	IDT	
Bacterial and virus strains		
AAV-DJ EF1a-DIO-GCaMP6f	Stanford	GVVC-AAV-93
AAV5.Syn.Flex.GCaMP6s.WPRE.SV40	Addgene	100845-AAV5
pGP-AAV-syn-jGCaMP7b-WPRE	Addgene	104489-AAV1
pAAV.Syn.GCaMP6s.WPRE.SV40	Addgene	100843-AAV9
pAAV-FLEX-tdTomato	Addgene	28306-AAV9
Chemicals, peptides, and recombinant proteins		
Cocaine	Sigma-Aldrich	C5776–1G
Normal Donkey Serum	Jackson Immune	017–000-121
Dimethyl sulfoxide	Fisher	D128–4
Heparin	Sigma-aldrich	H3393–100KU
Triton X-100	Sigma-aldrich	93443–100ML
TWEEN 20	Sigma-aldrich	3005
Glycine	Sigma-aldrich	G7126–100G
D-Fructose	Sigma-aldrich	F0127–1KG
1-Thioglycerol	Sigma-aldrich	M1753–100ML
Formamide	Millipore	344206–100ML
SSC	Thermofisher	AM9763
Tween-20	Sigma-aldrich	P9416
Ribonucleoside vanadyl complex	BioLabs	S1402S
Salmon sperm DNA	Thermo-Fisher	15632011

REAGENT or RESOURCE	SOURCE	IDENTIFIER
hairpins	Molecular Technologies	N/A
Experimental models: Organisms/strains		
VIP-cre X Ai162 (GC6s)	Jackson Laboratory Stock	010908, 031562
VIP-cre X Ai140 (GFP)	Jackson Laboratory Stock	010908, 30220
DAT-cre	Jackson Laboratory Stock	6660
TH-cre	EMMA, Ted Ebendal	254
C57BL/6N	Charles River	C57BL/6NCrl
Drd1-cre	Jackson Laboratory Stock	030989-UCD
Drd2-cre	Jackson Laboratory Stock	032108-UCD
Thy1-YFP	Jackson Laboratory Stock	3782
Software and algorithms		
ImageJ, version 2.0.0-rc-69/1.52n	NIH, open source	https://fiji.sc/
Adobe Illustrator, 24.0.2 (64-bit)	Adobe	https://www.adobe.com/products/illustrator.html
MATLAB R2018a, R2020b	MathWorks Inc.	https://www.mathworks.com/products/matlab.html
ABET II, Model 89501	Lafayette Instrument Company	https://lafayetteneuroscience.com/
Imaris 9.2.0	Oxford Instruments	https://imaris.oxinst.com/
Zen (LSM 880 with and without Airyscan, 2.3 lite)	Zeiss Microscopy	https://www.zeiss.com/corporate/int/home.html
BZ-X700 microscope and BZ-X Analyzer	Keyence	https://www.keyence.com
BioRender	BioRender	https://biorender.com/
LabVIEW 2016 (32bit)	National Instruments	https://www.ni.com/en-us.html
Custom code to analyze and generate figures	This paper	https://zenodo.org/record/5329620
Other		
Optical fiber, 400 μm diameter, 7 mm long	Doric Lenses	MFC_400/430–0.48_7mm_ZF1.25_FLT
Optical fiber, 400 μm diameter, 3 mm long (For distance visualization)	Doric Lenses	MFC_400/430–0.48_3mm_ZF1.25_FLT
Optical fiber, 200 μm diameter, 4 mm long (For distance visualization)	Doric Lenses	MFC_200/240–0.22_4mm_ZF1.25_FLT
Mono Fiberoptic Patch cable	Doric Lenses	MFC_400/430_0.48_2m_FC_ZF1.25_FL
GRIN lens, 500 μm diameter, 8.4 mm long	Inscopix	GLP-0584,
GRIN lens, 600 μm diameter, 7.3 mm long	Inscopix	GLP-0673
GRIN lens, 500 μm diameter, 8.85 mm long	GRIN-tech	NEM-050–30-10–920-S-2.0p
Custom ferrule for holding GRIN lens	Kientec Systems	FZI-LC-L2.5–520